Applied Catalysis B: Environmental 342 (2024) 123367

Contents lists available at ScienceDirect

Applied Catalysis B: Environmental

journal homepage: www.elsevier.com/locate/apcatb

Molecular elucidation of CO_2 methanation over a highly active, selective and stable $LaNiO_3/CeO_2$-derived catalyst by *in situ* FTIR and NAP-XPS

Jon A. Onrubia-Calvo [a], Sergio López-Rodríguez [b], Ignacio J. Villar-García [c], Virginia Pérez-Dieste [c], Agustín Bueno-López [b], Juan R. González-Velasco [a,*]

[a] Chemical Engineering Department, Faculty of Science and Technology, University of the Basque Country, UPV/EHU, Barrio Sarriena, s/n, E48940 Leioa, Bizkaia, Spain
[b] Department of Inorganic Chemistry, University of Alicante, Carretera San Vicente del Raspeig s/n, E-03080 Alicante, Spain
[c] ALBA Synchrotron Light Source, Carrer de la Llum 2–26, Cerdanyola del Vallès, 08290 Barcelona, Spain

ARTICLE INFO

Keywords:
CO_2 methanation
$LaNiO_3$ perovskite
CeO_2 support
NAP-XPS
in situ FTIR

ABSTRACT

The CO_2 methanation mechanism over the highly active (*TOF*=75.1 h^{-1}), selective (>92%) and stable 10% $LaNiO_3/CeO_2$-derived catalyst is still unresolved. The surface of the catalyst is monitored under hydrogenation (H_2), oxidizing (CO_2) and CO_2 methanation (H_2 +CO_2) conditions by near ambient pressure X-ray photoelectron spectroscopy (NAP-XPS) using synchrotron radiation. Meanwhile, the main reaction intermediates are identified by *in situ* FTIR analysis. NAP-XPS experiments confirm that $LaNiO_3$ perovskite reduction leads to the ex-solution of Ni^0 nanoparticles and Ni^{2+}—CeO_{2-x} and Ni^{2+}—La_2O_3 interfaces conformation, favouring the CO_2 adsorption and the H_2 dissociation/transfer. *In situ* FTIR experiments combined with the C1s spectra (NAP-XPS) suggest that the CO_2 activation occurs on CeO_{2-x} (oxygen vacancies and OH^-) at low temperatures, in the form of bi-carbonates; whereas, mono-/bidentate carbonates are formed on different strength La_2O_3 sites at increasing temperatures. These species are consecutively reduced to formates, as the main reaction intermediate, and methane by the H spilled from Ni^0 nanoparticles near to NiO—CeO_{2-x} and NiO—La_2O_3 interfaces.

1. Introduction

The exponential increase in the demand and consumption of fossil fuels has led to rising levels of CO_2 concentration in the atmosphere up to reach 420 ppm in 2022, which in turn results in global warming and environmental pollution [1,2]. To achieve the targets of the Paris Climate Convention, different technological alternatives are developed to enable a feasible and gradual transition from carbon-based to renewable fuels [3,4]. Over the past few years, CO_2 capture and utilization (CCU) technology has been regarded as one of the most promising strategies since it can be considered carbon-neutral, contributes to mitigate the fluctuations of renewable energies and significantly reduces the processing costs with respect to CO_2 capture and storage (CCS). One of the most viable and sustainable CCU alternative is the CO_2 valorisation in the form of methane (Eq. 1) [5], since this reaction does not require additional heat input and the synthetic natural gas (SNG) produced can be stored and transported through existing natural gas infrastructure [6–8].

$$CO_2 + 4H_2 \rightleftarrows CH_4 + 2H_2O \qquad \Delta H^0 = -164\ \text{kJ mol}^{-1} \qquad (1)$$

Reducing the eight electrons of CO_2 to CH_4 with hydrogen at low temperatures involves kinetic limitations. The pursuit of active and selective catalysts is essential to accelerate the reaction kinetics advancing towards industrial applications. Ni-based formulations usually present the best activity to cost ratio [9,10]. However, conventional preparation methods used for the synthesis of supported metal catalysts (*i.e.*, vapour infiltration and impregnation) often lead to large and heterogeneous particle size distribution [11]. As a result, Ni-based catalysts suffer from limited catalytic activity at low temperatures, metal sintering, oxidation at high temperatures and favour carbon deposits formation.

Considering the concept proposed by Daihatsu and Toyota [12], the *in situ* growth of Ni NPs from a perovskite host ($LaNiO_3$) has emerged as a promising strategy to obtain active, selective and stable catalyst for large-scale industrial applications involving the CO_2 methanation reaction [13]. Based on the promoting effect reported in the literature [14–22] for CeO_2-supported catalysts with respect to TiO_2-, Al_2O_3- and ZrO_2-supported counterparts, we recently explored the viability of supporting $LaNiO_3$ perovskites over CeO_2 (10–50% $LaNiO_3/CeO_2$) as a simple alternative for obtaining highly active and stable materials for

* Corresponding author.
E-mail address: juanra.gonzalezvelasco@ehu.es (J.R. González-Velasco).

https://doi.org/10.1016/j.apcatb.2023.123367
Received 1 July 2023; Received in revised form 23 September 2023; Accepted 6 October 2023
Available online 7 October 2023
0926-3373/© 2023 The Author(s). Published by Elsevier B.V. This is an open access article under the CC BY-NC-ND license (http://creativecommons.org/licenses/by-nc-nd/4.0/).

the CO_2 methanation reaction [23]. Specifically, the 10% $LaNiO_3/CeO_2$ precursor provided a catalyst with remarkably superior conversion of CO_2 to CH_4 and stability compared to that of the conventional Ni/CeO_2 catalyst in the CO_2 methanation reaction.

Several perovskite-derived formulations (Table 1) have been developed for the CO_2 methanation [24–38]. However, only preliminary mechanistic studies have been carried out on these novel materials. Wang et al. [25] suggest that the reaction towards CH_4 formation goes through the C–O dissociated of HCOO* species over $PdO/LaCoO_3$ catalyst. Re et al. [26] and Suk-Lim et al. [28] proposed CO route as the most plausible reaction mechanism for the CO_2 methanation on $La_{1.5}Ce_{0.5}NiO_4$–derived and $La_{1-x}Ca_xNiO_3$-derived (with x = 0–0.6) catalysts. Zhang et al. [31] proposed that the Ce incorporation in the $Al_{1-x}Ce_xNiO_3$ (with x = 0, 0.1, 0.2 and 0.4) structure modifies the CO_2 methanation mechanism from CO route to formate intermediate pathway. Do et al. [37] preliminary analyzed the reaction intermediates on $Ni_{1-x}Ca_xTiO_3/Al_2O_3$-derived catalyst and suggest that CO_2 methanation occurs by a combination of CO and formate routes, in which formates are firstly formed from carbonates adsorbed on CaO and, then, dissociated to CO, which is consecutively hydrogenated to COH → CH_2O → CH_3O → CH_3OH → CH_4. However, these studies are usualy based on common characterization techniques, such as CO_2-TPD as well as *ex situ* XPS and/or DRIFT/FTIR spectroscopies. As a result, the CO_2 methanation mechanism on these novel materials and the detailed roles of different active phases still remain unclear and strongly depends on catalyst composition.

In situ studies are essential for detecting surface reaction intermediates and active phases that are present under the reaction conditions [39]. In this regard, the dynamic of the main reaction intermediates involved in the reaction pathway can be identified through *in situ* FTIR experiments. On the other hand, *in situ* near ambient pressure X-ray photoelectron spectroscopy (NAP-XPS) with synchrotron radiation is a powerful tool to identify the chemical states of the active catalysts under different reaction conditions, which aids in revealing the catalytic reaction pathways [40–43]. Considering this background, the combination of *in situ* NAP-XPS and FTIR experiments under simulated reaction conditions could be a smart solution to elucidate CO_2 methanation mechanism over these novel formulations.

Herein, we report a thorough mechanistic investigation of the CO_2 methanation reaction on highly active, selective and stable 10% $LaNiO_3/CeO_2$-derived catalysts using advanced techniques, such as *in situ* NAP-XPS and FTIR. Special attention was paid on identifying the nature of different active sites and the role of different intermediates to propose the dominant CO_2 methanation pathway over the novel 10% $LaNiO_3/CeO_2$-derived catalyst. These insights into the reaction mechanism may be of great help to develop a kinetic model that could accurately predict the catalytic behaviour of this novel catalyst for CO_2 methanation under industrially relevant conditions and for designing novel formulations with enhanced activity, selectivity and stability in the CO_2 methanation reaction.

Table 1
Overview of perovskite-based precursors reported in the literature as well as their corresponding Ni contents (*Ni*), weight hourly space velocities in the literature for the CO_2 methanation (*WHSV*), temperatures at which a 50% CO_2 conversion is obtained (T_{50}) and turnover frequencies (TOF).

Formulation	*Ni*, %	*WHSV*, L g^{-1} h^{-1}	T_{50}, °C	*TOF*, h^{-1} *	Reference
$LaFe_{0.8}Ni_{0.2}O_3$	4.9	30.0	460	n.a.	[24]
$PdO@LaCoO_3$	n.a.	18.0	n.a	n.a.	[25]
$La_{0.5}Ce_{1.5}NiO_4$	11.2	1.1	275	n.a.	[26]
$LaCo_{0.7}Ni_{0.3}O_3$	n.a.	2.4	n.a.	n.a.	[27]
$La_{0.6}Ca_{0.4}NiO_3$	27.3	16.2	272	91.7 (235 °C)	[28]
$LaKNiO_3$	26.9	48.0	240	n.a.	[29]
$Rh/LaAl_{0.92}Ni_{0.08}O_3$	n.a.	48.0	280	15.8 (330 °C)	[30]
$Al_{0.8}Ce_{0.2}NiO_3$	48.9	48.0	185	18.1 (175 °C)	[31]
$Ni/CaTiO_3$	2.2	48.0	260	n.a.	[32]
30% $LaNiO_3/SiO_2$	9.4	6.0	245	n.a	[33]
30% $LaNiO_3/SiO_2$ (MCF)	9.3	60.0	325	n.a	[34]
$LaNi_{0.83}Mo_{0.17}O_3/SiO_2$	5.9	15.0	280	65.9 (200 °C)	[35]
$LaNi_{0.95}Co_{0.05}O_3/SiO_2$ (MCF)	20.0	60.0	370	n.a	[36]
$Ni_{0.95}Ca_{0.05}TiO_3/Al_2O_3$	11.0	0.6	365	68.4 (400 °C)	[37]
$La_{0.9}Ce_{0.1}NiO_3/ZrO_2$	7.2	15.0	232	17.3 (200 °C)	[38]
10% $LaNiO_3/CeO_2$	2.8	30.0	315	75.1 (250 °C)	This work

* Estimated according to Eq. 5.

2. Experimental

2.1. Preparation and characterization of the perovskite-based precursor

The 10% $LaNiO_3/CeO_2$ precursor was prepared by combining citric acid and impregnation methods, as reported elsewhere [23]. Briefly, a cerium oxide support was obtained by direct calcination of the $Ce(NO_3)_3{\cdot}6\,H_2O$ (*Sigma Aldrich,* 99.9%) precursor for 4 h at 500 °C in static air. Once CeO_2 was obtained, stoichiometric amounts of $La(NO_3)_2{\cdot}6\,H_2O$ (*Merck,* 99.0%) and $Ni(NO_3)_2{\cdot}6\,H_2O$ (*VWR*, 99.9%) were dissolved in distilled water under vigorous stirring. Then, citric acid ($C_6H_8O_7{\cdot}H_2O$, *Sigma Aldrich,* 99%) was added as a complexing agent with a citrate to nitrate molar ratio of 1.1, and the pH value was adjusted by ammonia water (25% as NH_3, *Panreac*) to a value of 7. After that, the resulting solution was added to the ceria support inside a rotary evaporator (under vacuum at 35 °C) to obtain a homogeneously distributed gel precursor over the ceria support. The obtained gel was further dried at 120 °C overnight. Finally, the desired 10% $LaNiO_3/CeO_2$ precursor was obtained after calcining the dry gel for 4 h at 600 °C under a flow of 5% O_2/He. Corresponding characterization results are summarized in the Supporting Information, including X-ray diffraction (XRD, Fig. S1), N_2 adsorption-desorption (Fig. S2 and Table S1), STEM-EDS mapping (Fig. S3), temperature programmed desorption of H_2 (H_2-TPD, Fig. S4 and Table S1) and CO_2 (CO_2-TPD, Fig. S5 and Table S2).

2.2. Catalytic activity and stability

CO_2 methanation reactions were conducted in a down flow fixed-bed reactor (D_{in} = 9 mm). For that, 0.5 g (d_p = 0.3–0.5 mm) of the 10% $LaNiO_3/CeO_2$ precursor was mixed with quartz particles (0.5–0.8 mm) to reach a total volume of 1 mL. To ensure the complete reduction of the $LaNiO_3$ perovskite and, as a consequence, the controlled Ni NP exsolution, the 10% $LaNiO_3/CeO_2$ precursor was reduced *in situ* at 550 °C for 2 h under a 20% H_2/He mixture (250 mL min^{-1}). After cooling to 200 °C in He, the CO_2 methanation reaction was performed by introducing the reaction mixture at atmospheric pressure. The feed stream consisted of a 250 mL min^{-1} H_2/CO_2/He mixture with a 4:1:1.25 molar ratio. These conditions result in a space velocity (GHSV) of 15,000 h^{-1} and a space time (W/F_{A0}) of 4.67 g_{cat} h mol^{-1}. During the catalytic test, the temperature was increased from 200° to 500°C in steps of 25 °C, with a heat increase in 5 °C min^{-1} between each step. The He, H_2, CO_2, CH_4 and CO concentrations at the reactor exit were monitored once a steady state was reached at each temperature by a gas chromatograph (*Agilent 490 micro GC*).

The CO_2 conversion (X_{CO_2}) and the selectivity towards CH_4 (S_{CH_4}) and CO (S_{CO}) were calculated according to the following equations:

$$X_{CO_2} = \frac{F^{in}_{CO_2} - F^{out}_{CO_2}}{F^{in}_{CO_2}} \quad (2)$$

$$S_{CH_4} = \frac{F^{out}_{CH_4}}{F^{out}_{CH_4} + F^{out}_{CO}} \quad (3)$$

$$S_{CO} = \frac{F^{out}_{CO}}{F^{out}_{CH_4} + F^{out}_{CO}} \quad (4)$$

where $F^{in}_{CO_2}$ and $F^{out}_{CO_2}$ are the molar CO_2 flow (mol h^{-1}) at the reactor inlet and outlet, respectively. Similarly, F^{out}_{CO} and $F^{out}_{CH_4}$ are the molar CO and CH_4 flows (mol h^{-1}) at the reactor outlet, respectively.

The activity of the 10% $LaNiO_3/CeO_2$-derived catalyst on the CO_2 methanation reaction was further investigated by measuring the apparent turnover frequency (*TOF*). The *TOF* (h^{-1}) for CO_2 conversion, defined as the number of converted CO_2 molecules per surface metallic Ni active site per second, was calculated by the following equation:

$$TOF = X_{CO_2} F^{in}_{CO_2} \frac{M_{Ni}}{W \cdot Ni \cdot D} \quad (5)$$

where X_{CO_2} is the CO_2 conversion at 250 °C, $F^{in}_{CO_2}$ (mol h^{-1}) is the CO_2 flow rate, *W* is the catalyst mass (g), *Ni* is the Ni mass fraction determined by ICP—AES, *D* is the Ni dispersion estimated by H_2-TPD, and M_{Ni} is the molecular weight of Ni (58.69 g mol^{-1}). Note that the calculation of the *TOF* was conducted with data in the range of CO_2 conversion below 15% under simulated differential reactor conditions for better accuracy and to avoid mass transport limitation.

Finally, the stability of the 10% $LaNiO_3/CeO_2$-derived catalyst was evaluated by automatically analysing the outlet He, H_2, CO_2, CH_4 and CO concentrations for 72 h at 325 °C. Note that the feed composition was the same as that used during previous activity tests.

2.3. *In situ NAP-XPS experiments*

In situ near ambient pressure X-ray photoelectron spectroscopy (NAP-XPS) was performed at the NAP branch of the CIRCE beamline at the ALBA Synchrotron Light Source, which is able to operate with tunable photon energy ranging between 100 and 2000 eV using a SPECS PHOIBOS NAP150 energy analyser (SPECS GmbH). The beamspot size was 100 × 20 μm^2 (HxV). The spectra were acquired with a 20 eV pass energy and 0.05 eV energy step. Specifically, photon energy values of 1125, 320 and 375 eV were used to monitor the Ce 3d, Ce 4d and Ni 3p regions at different depths. The corresponding inelastic mean free paths (IMFP) for pure solid phases of NiO and CeO_2 are summarized in Table S4 [44].

The 10% $LaNiO_3/CeO_2$ powder precursor was pelletized and placed on a gold mesh to prevent surface charging and provide a Au4f peak as a reference. Notably, catalytic activity of the gold mesh was experimentally ruled out. An infrared laser system (808 nm) was used to heat the samples with a constant heating ramp of 10 °C min^{-1}. Temperature control was carried out by a K-type thermocouple. The pressure in the analysis chamber was maintained at 1 mbar during the whole set of experiments, whereas the total gas flow was set at 30 mL min^{-1} in all experiments. The gas phase composition was monitored during the whole experiment by a mass spectrometer (MKS Instruments) installed at the second stage of the differential pumping analyser. C 1 s transition at 284.6 eV was used as an internal reference to adjust the binding energy scale of peaks obtained for the experiments carried out with 320 and 375 eV photon energy, whereas the Ce 3d transition at 916.7 eV was used for the experiments carried out with 1125 eV photon energy.

Fig. 1 shows the experimental protocol followed during NAP-XPS experiments. Note that XPS spectra were recorded at each temperature level and/or feed stream composition specified once the steady-state was reached (around 60 min). First, the catalyst was pretreated in pure H_2 (30 mL min^{-1}) from 150 °C to 500 °C (2 h). Different spectra were recorded at each temperature (step 1) in intervals of 50 °C. Then, the sample was cooled to 200 °C in H_2, and the methanation mixture containing 20% CO_2 (6 mL min^{-1}) + 80% H_2 (24 mL min^{-1}) was fed to the analysis chamber (step 2). The temperature was increased from 200 °C to 450 °C in intervals of 50 °C, and different spectra were recorded at each temperature level. After these measurements under CO_2 methanation conditions, the system was cooled to 150 °C in a CO_2 methanation mixture (step 2), and then, the temperature was increased to 300 °C in pure CO_2 (step 3, 30 mL min^{-1}). Finally, the gas mixture composition was switched in isothermal conditions as follows: pure H_2 (30 mL min^{-1}, step 4) and 20% CO_2 + 80% H_2 (6 mL min^{-1} + 24 mL min^{-1}, step 5).

2.4. *In situ FTIR experiments*

In situ FTIR were carried out in a Cary 600 Series FTIR spectrometer (Agilent) coupled with a high-temperature cell equipped with ZnSe windows (Specac), a gas inlet and outlet system and a cooling system. Spectra were collected by 52 scans in the range of 4000–400 cm^{-1} and a resolution of 4 cm^{-1}. Powdered samples (approximately 30 mg) were pressed at 2.0 tons into 10 mg cm^{-2} wafers. Prior to the experiments, pelletized samples in the form of discs were placed in a holder inside the cell and were *in situ* activated/reduced at 500 °C for 1 h under a 5% H_2/N_2 flow of 200 mL min^{-1}. After pretreatment, wafers were cooled under N_2 flow to 150 °C, and background spectra were collected every 50 °C as

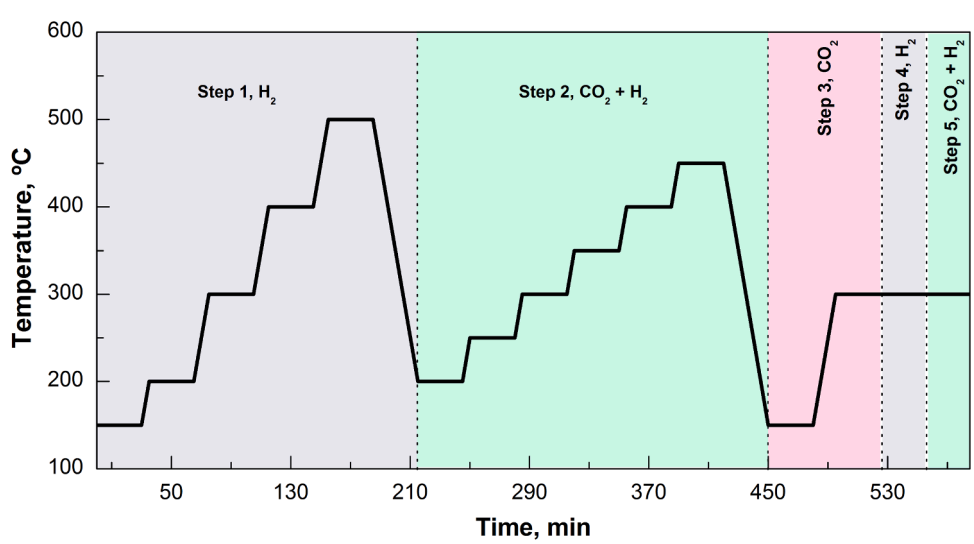

Fig. 1. Scheme of the protocol followed during the NAP-XPS experiments.

long as the temperature increased to 450 °C using a heating rate of 10 °C min^{-1}.

CO_2 adsorption and CO_2 methanation tests were carried out by exposing pretreated samples to a gas mixture of 312 mL min^{-1} composed of 5% CO_2/N_2 or 0.1% CO_2:0.4% H_2:99.5% N_2, respectively. For that, the corresponding gas mixture was fed to the gas cell for 30 min, while spectra were recorded as a function of time at each temperature level. Note that the depicted spectra were obtained by subtraction of those recorded under reaction/adsorption conditions every 50 °C and those corresponding to backgrounds recorded under N_2, whereas the heating increase between temperatures was carried out under N_2. Finally, the spectra were processed with Agilent Resolution Pro software, through which the background spectra recorded at each temperature level was subtracted.

3. Results and discussion

3.1. Catalytic activity, selectivity and stability

The high activity of the catalyst derived from the 10% $LaNiO_3/CeO_2$ precursor is confirmed by the low temperature (315 °C) at which a 50% (T_{50}) CO_2 conversion is obtained (Fig. 2a). Furthermore, almost all CO_2 is converted into CH_4, since the selectivity towards this compound is above 92% (red line) in the whole temperature range, and almost of 100% below 425 °C. These values are in the range of those reported in the literature for similar formulations (Table 1). However, comparing the catalytic activity in terms of turnover frequency (*TOF*) for CO_2 conversion, here developed formulation shows a *TOF* value (75.5 h^{-1}) significantly higher than most of the reported values in the literature, which denotes its high intrinsic activity.

Based on characterization results (Figs. S1-S5 and Tables S1-S3), the high activity of this novel formulation is ascribed to an enhancement in textural properties and homogeneous Ni NP distribution with respect to bulk samples, which promotes the accessibility to weak and medium strength basic sites for CO_2 adsorption (CeO_2, Ni—CeO_{2-x} interface and highly dispersed La_2O_3) as well as to those implied in CO_2 methanation (Ni^0). Ultimately, these properties promote a closer proximity between the active sites involved in CO_2 activation and H_2 dissociation. As a result, the H_2 transfer from the Ni^0 sites to convert the adsorbed CO_2 into CH_4 [45,46] is favoured in line with the higher activity shown by this sample with respect to the CeO_2 support and the bulk perovskite ($LaNiO_3$) in Fig. S6.

Finally, the conformation of highly dispersed Ni NPs in close contact with La_2O_3 and CeO_2 phases on the Ni–La_2O_3/CeO_2 catalyst obtained after reduction step (Fig. S3) prevent it from the agglomeration, which increases its stability during long-term experiments (Fig. 2b). Thus, the combined high activity, selectivity towards methane and stability denotes the real superiority of the formulation object of study.

Considering the promising perspectives discovered thus far and aiming to advance the scale-up of this advanced formulation, the reaction mechanism and the role of the different active sites during the CO_2 methanation reaction over the novel 10% $LaNiO_3/CeO_2$-derived catalyst have been studied in the following sections by *in situ* NAP-XPS and *in situ* FTIR experiments.

3.2. In situ NAP-XPS characterization

Prior to *in situ* NAP-XPS analysis, the surface elemental composition and oxidation states of different species present in the fresh 10% $LaNiO_3/CeO_2$ precursor have been analysed by *ex situ* X-ray photoelectron spectroscopy (XPS, Fig. 3). The atomic relative contents of each compound at the surface determined after the deconvolution of the spectra (Table S3) have been used as reference during *in situ* NAP-XPS analysis.

Ni^0, Ni^{2+} and Ni^{3+} oxidation states were analyzed in the Ni 3p region (Fig. 3a), since the Ni $2p_{3/2}$ lines strongly overlap with the La $3d_{3/2}$ satellite line [47,48]. It is widely accepted [48–52] that the standard binding energy positions of Ni^{3+} $3p_{3/2}$, Ni^{2+} $3p_{3/2}$ and Ni^0 $3p_{3/2}$ peaks are 69.0, 67.3 and 66.3 eV, respectively. As can be observed in Fig. 3a, the Ni 3p transition presents several contributions between these standard positions. This fact suggests the coexistence of $Ni^{3+}/Ni^{2+}/Ni^0$ species. However, the absence of contributions below 67 eV discards the presence of Ni^0 in the fresh 10% $LaNiO_3/CeO_2$ precursor, which confirms that the perovskite is fully oxidized after the calcination step. Indeed, the Ni^{3+} and Ni^{2+} percentages in the fresh sample, determined after the deconvolution and integration of the different contributions, are 42% and 58% (Table S3), respectively.

Regarding to the Ce $3d_{5/2}$ spectrum (Fig. 3b), it presents the 10 components of Ce^{4+} and Ce^{3+} species [53–55]. Their relative proportion can be determined after the integration of different components, as reported elsewhere [56]. Specifically, the relative content of Ce^{4+} at the surface of the fresh sample is 87% (Table S3), which denotes the high oxygen storage capacity (OSC) of the ceria support.

Finally, the O 1 s spectrum (Fig. 3c) shows three components ascribed to: the surface lattice oxygen bonded to metallic cations accommodated within the crystal structure of the perovskite or ceria support (O^{2-}_{latt}, 528.8 eV); surface adsorbed oxygen on surface segregations or oxygen vacancies (O_{ads}, 531.2 eV); and water and hydroxyl groups on the surface (534.0 eV) [17], respectively. Meanwhile, the typical peaks of La^{3+} ions accommodated within the perovskite lattice can be identified in the La 3d region (Fig. 3d) [34,35].

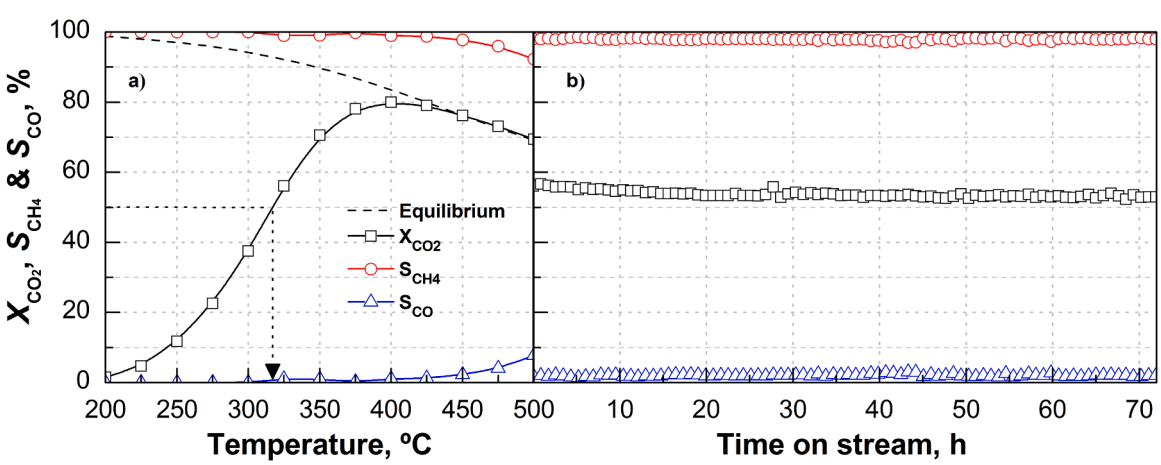

Fig. 2. Evolution of CO_2 conversion (X_{CO_2}) and selectivity towards CH_4 (S_{CH_4}) as well as CO (S_{CO}) as a function of a) reaction temperature and b) time on stream (325 °C) for the 10% $LaNiO_3/CeO_2$-derived catalyst.

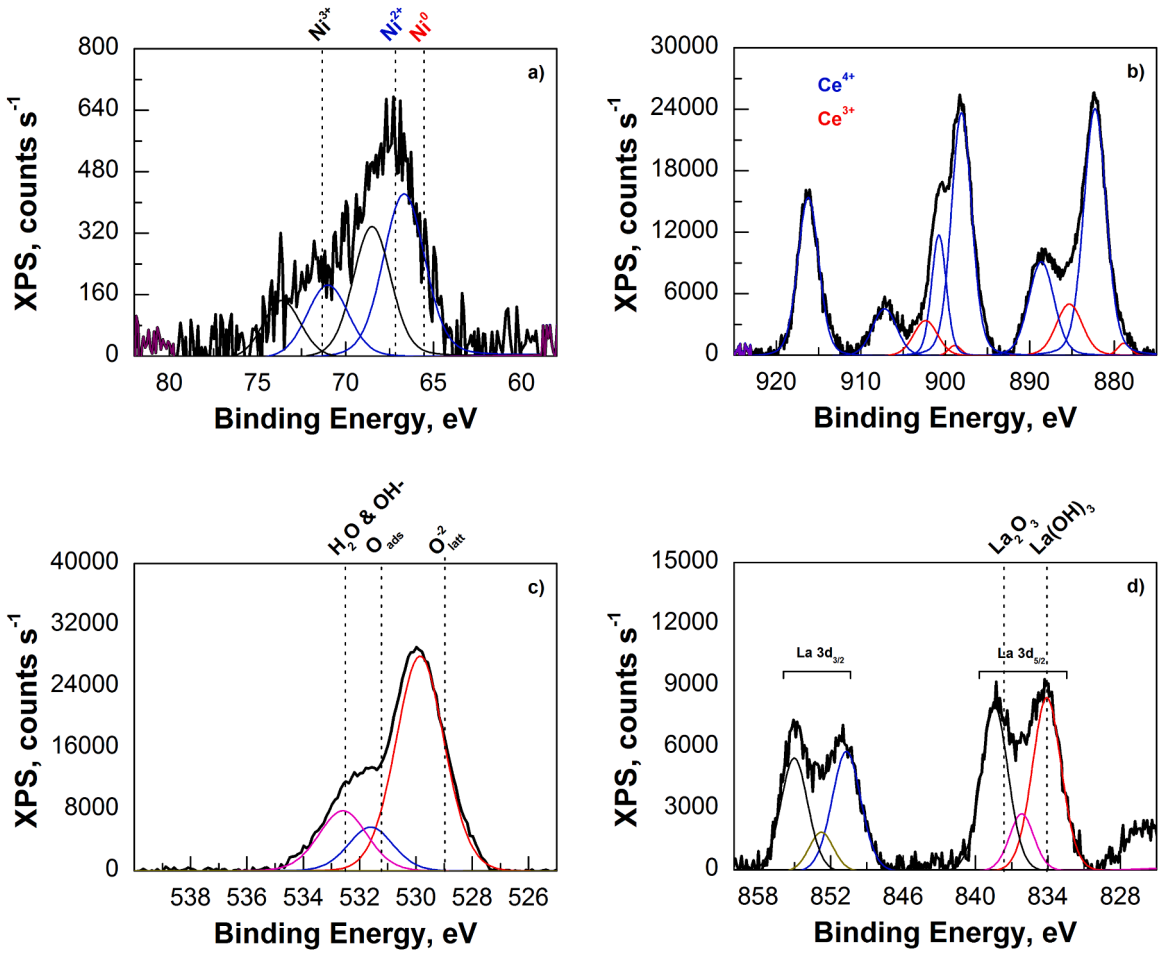

Fig. 3. *Ex situ* XPS spectra of a) Ni 3p, b) Ce 3d, c) O 1 s and d) La 3d transitions for the fresh 10% $LaNiO_3/CeO_2$ precursor.

3.3. *In situ NAP-XPS experiments during prereduction*

Following the evolution of Ce as well as Ni species during reduction pretreatment is of great interest to understand the evolution and changes experimented by perovskite-based precursors during reduction pretreatment up to the desired catalyst conformation. Fig. 4 shows the *in situ* NAP-XPS spectra recorded during the prereduction treatment (step 1 in Fig. 1) at increasing temperatures for the Ni 3p and Ce 3d regions as well as their corresponding deconvolution using a Shirley background and a combined Lorentzian-Gaussian function.

The Ni 3p transition can be deconvoluted into different peaks corresponding to Ni^{3+}, Ni^{2+} and Ni^0 species. However, the peak position as well as the distribution of different contributions is affected by the temperature of the reduction pretreatment (Fig. 4a). Similar to the fresh sample (Fig. 3a), no peaks ascribed to Ni^0 can be identified in the spectra recorded at 150 °C. In contrast, the peaks corresponding to Ni^{2+} (blue line) and Ni^{3+} (black line) species can be observed at this temperature. Above 200 °C, an increasing peak (red line), with its corresponding satellite, can be observed at approximately 65.5 eV, denoting the progressive formation of Ni^0 nanoparticles. Meanwhile, the Ni^{3+} peak (black line) completely vanishes at 200 °C due to its complete reduction to Ni^{2+} and Ni^0. As a result of this process, the starting perovskite-based precursor begins to disappear. Furthermore, a progressive shift of the Ni 3p peak towards lower BE can be identified at increasing temperatures. Indeed, the binding energy position of the metallic Ni peak is slightly lower than the values reported in literature (66.2 ± 0.15 eV) [49,57], especially at high temperatures. This trend denotes a higher negative charge density due to the strong interaction of nickel with La_2O_3 and/or CeO_2 phases [51], property that favours H_2 dissociation during the methanation reaction and the stability of the sample during long-term experiments (Fig. 2b) [17,58].

In the Ce 3d region (Fig. 4b) the characteristic 10 peaks of the Ce^{3+} (red line) and Ce^{4+} species (blue line) can be identified [53–55]. However, noticeable changes can be observed in the different peaks distribution, which suggests that the reduction pretreatment alters the Ce^{3+}/Ce^{4+} ratio.

In order to follow the proportion of different Ni and Ce species on the catalyst's surface, the deconvoluted peaks were grouped in different species for the quantification. Fig. 5 shows the evolution of the Ni and Ce species proportions with temperature during the reduction pretreatment under pure H_2 (step 1).

The Ni^{3+}, Ni^{2+} and Ni^0 species proportions are 37%, 63% and 0% at 150 °C (Fig. 5a), respectively. However, the increase in temperature to 200 °C leads to a complete reduction in Ni^{3+} species, as previously mentioned, and to a decrease in the Ni^{2+} proportion from 63% to 54%, resulting in a significant increase (46%) in Ni^0 content. Above this temperature, the Ni^0 species proportion continuously increases up to reach 70% at 500 °C. Thus, the Ni^{3+}/Ni^{2+} species previously identified for fresh samples are consecutively reduced to Ni^{2+} and then to Ni^0 during the pretreatment protocol, which is good agreement with the reduction peaks observed in Fig. 5c and the corresponding reduction stages (Eqs. 6–8) previously reported [59].

$$4LaNiO_3 + 2H_2 \rightarrow La_4Ni_3O_{10} + Ni^0 + 2H_2O \quad (6)$$

$$La_4Ni_3O_{10} + 3H_2 \rightarrow La_2NiO_4 + 2Ni^0 + La_2O_3 + 2H_2O \quad (7)$$

$$La_2NiO_4 + H_2 \rightarrow 2Ni^0 + La_2O_3 + H_2O \quad (8)$$

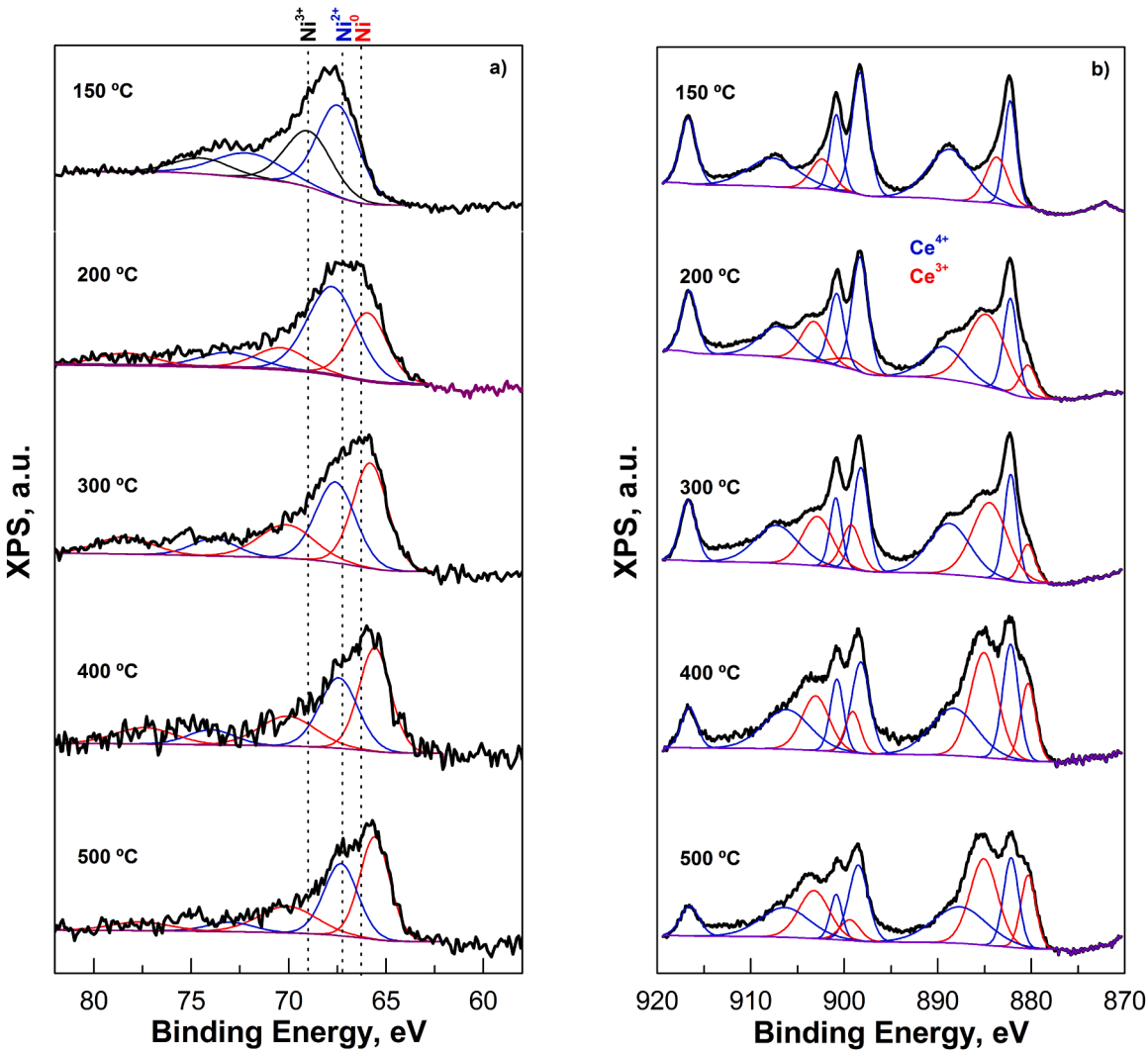

Fig. 4. *In situ* NAP-XPS spectra recorded for the 10% $LaNiO_3/CeO_2$ precursor with a 1125 eV photon energy in the a) Ni 3p and b) Ce 3d transitions during reduction pretreatment in H_2 at increasing temperatures (step 1).

At the same time, the Ce^{3+} proportion progressively increases from 16% to 41% (Fig. 5b). This trend denotes the progressive reduction of Ce^{4+} in the CeO_2 support, leading to the conformation of oxygen vacancies at the surface (Eq. 9). However, a 59% of Ce^{4+} is still present after the reduction pretreatment at 500 °C. In agreement with the H_2-TPR results (Fig. 5c), only surface Ce^{4+} can be reduced in this temperature range, and therefore, higher temperatures are necessary to complete the reduction of bulk CeO_2 [60].

$$2CeO_2 + H_2 \rightarrow Ce_2O_3 + H_2O \quad (9)$$

It is worth mentioning that, although Ni and ceria are not completely reduced, the reduction peaks of different Ni-containing species and ceria support shift to lower temperatures with respect to those observed for the bulk perovskite ($LaNiO_3$) and CeO_2 included as reference in Fig. 5c. This fact suggests an intimate contact between perovskite and support, which promotes the accessibility of the former and the reducibility of the latter due to a spillover effect of activated H_2 [61]. As a consequence, the conformation of NiO—CeO_{2-x} mixed oxide is suggested [41].

In summary, the *in situ* NAP-XPS experiments carried out during precursor reduction confirm that; initially, the fresh perovskite-based precursor is highly oxidized. However, $LaNiO_3$ perovskite and CeO_2 support are progressively reduced as long as the sample is treated under pure H_2 at increasing temperature. As a result, a mix between Ni^0 NPs distributed over the La_2O_3 and CeO_2 surfaces with Ni^{2+}—CeO_{2-x} and Ni^{2+}—La_2O_3 mixed oxides is expected at the end of the reduction pretreatment. This aspect was confirmed by STEM-EDS images obtained for the sample after reduction and reaction steps (Fig. S3), where Ce (blue colour) and La (green colour) elements coexist with a homogeneous distribution in all the analyzed areas with small-sized (≈ 1.5 nm) Ni NPs (red colour) uniformly dispersed over their surface. In agreement with the observed in our previous work [26], these structural changes lead to a decrease of Ni/Ce and La/Ce ratios at the surface with respect to those observed for the fresh perovskite-based precursor.

3.4. *In situ NAP-XPS experiments during CO_2 methanation*

Once the desired catalyst was conformed (step 1), the reaction chamber was cooled to 200 °C and; then, the CO_2 methanation mixture (20% CO_2 and 80% H_2) was fed to the sample (step 2 in Fig. 1). The temperature was increased from 200° to 450°C, in steps of 50 °C, and XPS spectra were recorded at each reaction temperature after sample saturation and repetitive spectra were obtained (60 min). Note that 3 different photon energies (320, 375 and 1125 eV) were used to determine different compounds proportions at increasing depths (Table S4).

Fig. 6 shows the evolution of Ni^0 and Ce^{3+} proportions with temperature during the CO_2 methanation reaction at different depths. These values were determined from XPS spectra recorded in the Ni 3p and Ce 4d regions with 1125 eV (Fig. S7) as well as 320 and 375 eV (Fig. S8)

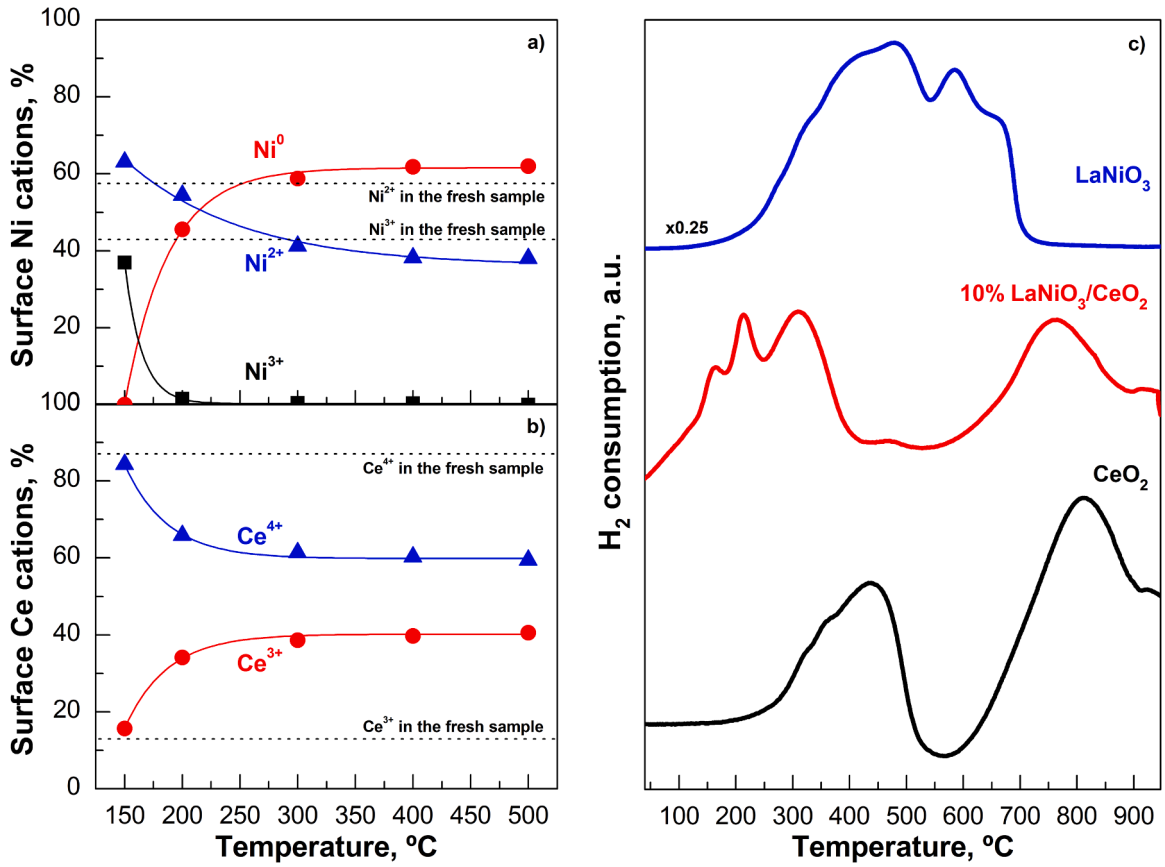

Fig. 5. Evolution with temperature of a) the Ni and b) Ce species contents during reduction pretreatment in H_2 (step 1, 1125 eV) as well as c) H_2 consumption profile during the H_2-TPR experiment for the fresh 10% $LaNiO_3/CeO_2$ precursor. Reference dotted lines indicate the percentage of different species in the fresh 10% $LaNiO_3/CeO_2$ precursor obtained by ex situ XPS analysis.

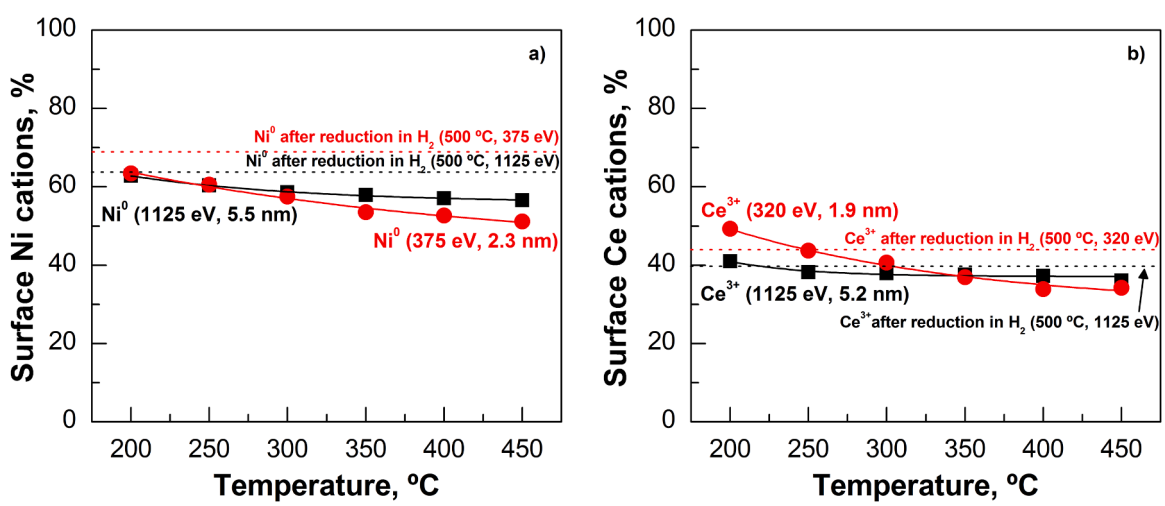

Fig. 6. Evolution with temperature of a) Ni^0 and b) Ce^{3+} contents relative to the total nickel and cerium contents, measured by NAP–XPS experiments during the CO_2 methanation reaction (20% CO_2 and 80% H_2). The photon energies and probed depths (estimated as 3 times the inelastic mean free path, IMFP) are also indicated. Reference dotted lines indicate the percentage of different species after step 1 (reduction in H_2 at 500 °C).

photon energies. As can be observed, the Ni^0 content, obtained after the reduction treatment at 500 °C, is higher at more superficial layers (69%) than at deeper regions (64%). This observation indicates that more superficial Ni nanoparticles are easily reduced, which probably leads to a weaker contact with the other phases. Regardless, the presence of partially oxidized Ni, even at more superficial regions, denotes its stabilization inside the NiO—CeO_{2-x} interface as suggested by H_2-TPR experiments (Fig. 5c). Based on the characterization results (Figs. S3 and S4 as well as Table S1), this observation is ascribed to the conformation of small Ni^0 nanoparticles with homogeneous size, which favours their uniform interaction with the ceria support.

After exposure to the CO_2 methanation gas mixture at 200 °C (Fig. 6a), the metallic nickel proportion in deeper regions (incident energy of 1125 eV) is only slightly reduced (63%) relative to the initial

state (dotted black lines, 64%), which indicates the high stability of Ni^0 NPs in line with the low deactivation degree observed during long-term experiments (Fig. 2b). In contrast, the Ni^0 percentage decreases in higher extent (from 69% to 64%) for the more superficial sites, suggesting that the Ni^0, nearer to the external surface, is more easily oxidized under the reaction environment ($CO_2 + H_2$).

Regarding to Ce contents, a noticeable increase in the Ce^{3+} content can be observed for the 320 eV incident energy. Specifically, this parameter increases from 44%, after reduction pretreatment, to 49% at 200 °C (Fig. 6b). This trend suggests that the reduction of Ce^{4+} near to the surface continues during the cooling stage under pure H_2, in line with the reduction process proposed for ceria support after theanalysis of the H_2-TPR results (Fig. 5c).

Above 200 °C, a progressive reoxidation of Ni and Ce is observed with respect to the previous H_2 reduction pretreatment, irrespective of the incident energy. Specifically, the Ni^0 relative content decreases from 63% (200 °C) to 57% (450 °C) for the 1125 eV incident energy, with a proportional increase in the Ni^{2+} percentage. As expected, this decrease is higher (from 64% to 51%) for the Ni^0 sites closer to the surface. On the other hand, the Ce^{3+} percentage decreases by 5% and 15% from 200 °C to 450 °C for the 1125 and 320 eV incident energies, respectively.

In order to gain insight on these results, the C1s region has been also analyzed during the exposure to CO_2 mixture. Fig. 7a shows the spectra recorded in the C1s region under CO_2 methanation mixture at increasing temperatures. The C1s spectrum recorded after reducing pretreatment has been also included as reference.

As can be observed, multiple peaks can be identified in this region, which can be assigned to the presence of different carbon-based species. The main peak (284.6 eV) detected is due to adventitious aliphatic carbon [62]. Note that this peak was used to calibrate the XPS peaks obtained with 320 and 375 eV incident energies. Furthermore, a strong peak can be observed near 290.2 eV, which is attributed to adsorbed CO_x species in form of surface carbonates (CO_3*) species [63,64]. It is worth to mention that this peak is identified even after H_2 pretreatment at 500 °C, denoting the presence of highly stable carbonates in the sample.

In agreement with the decreasing trend observed for Ce^{3+} in Fig. 6, it is widely accepted that ceria is able to chemisorb and dissociate CO_2 ($CO_2 \rightarrow CO + O^*$), even at 200 °C. Thus, it can be assumed that CO_x species adsorption during CO_2 methanation leads to an exchange of oxygen atoms with the ceria support leading to the partial oxidation of Ce^{3+} to Ce^{4+} [41,65]. This process mainly takes place on the oxygen vacancies near or at the surface, which are formed due to the partial reduction of the CeO_2 support during the reduction pretreatment (Fig. 5c) [66]. As observed in Fig. 6a, CO_2 adsorption also contributes to Ni^0 reoxidation, since a considerable percentage of Ni^{2+} (> 30%) is present, even at low-intermediate temperatures. Considering that no carbonyls are detected, this process may occur throughout O* transfer from CeO_2 at the NiO—CeO_{2-x} interface. However, there is much more ceria than nickel in the sample; therefore, it can be assumed that the oxygen generated upon CO_2 dissociation or H_2O adsorption in the form of hydroxyls, preferentially refills the oxygen vacancies of the ceria support instead of accumulating on nickel, highlighting the key role of ceria as an oxygen reservoir. These results suggest the participation of ceria support in CO_2 dissociation and activation [64].

It is worth noting that a saturating trend can be observed in the Ce^{3+} proportion at higher temperatures, which denotes that the progressive increase in Ce^{4+} percentage partially limits the CO_2 adsorption on oxygen vacancies [67,68], whereas the Ni^0 reoxidation continues at high temperatures. This trend suggests that some oxygen is still transferring between the catalyst surface and Ni^0 NPs due to an alternative mechanism. Based on the results reported in our previous work [69] and those observed in CO_2-TPD experiments (Fig. S5 and Table S2), CO_2 adsorption on La_2O_3 sites, instead of on the ceria support, is favoured at increasing temperatures. Note that a minor carbonates peak is still present in the C1s at 450 °C (Fig. 7a). Thus, Ni^0 sites reoxidation might continue throughout O* transfer from La_2O_3 sites at the NiO—La_2O_3

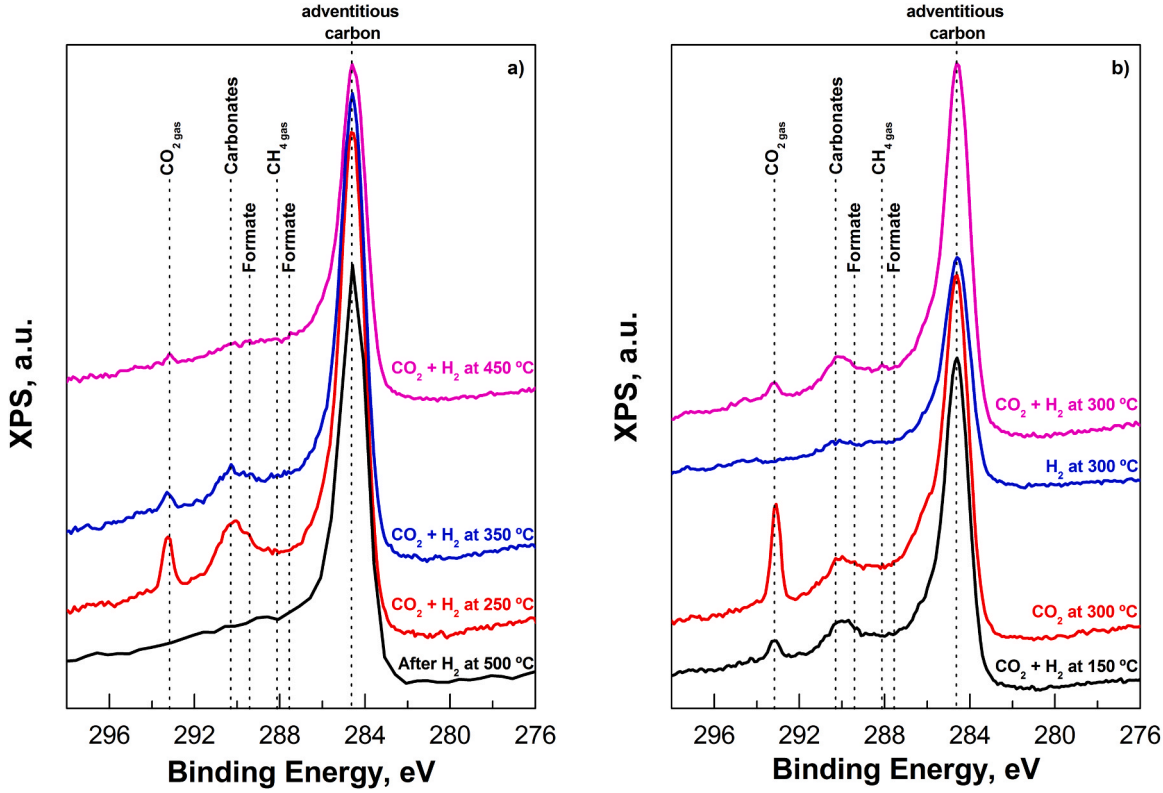

Fig. 7. *In situ* NAP-XPS spectra recorded for the 10% $LaNiO_3/CeO_2$-derived catalyst with a 375 eV photon energy in the C1s transition during a) CO_2 methanation at increasing temperatures (step 2) and b) experiments under switching gas atmosphere (steps 3–5).

interface at high temperatures.

Regardless, a high proportion of Ni^0 nanoparticles (> 51% at 375 eV) can be identified irrespective of the reaction temperature. Indeed, the Ni^0 percentage detected in the sample below 400 °C is significantly higher than that previously reported (< 50%) for the conventional Ni/CeO_2 catalyst [41]. This behaviour is ascribed to the controlled exsolution of the Ni^0 NPs from the perovskite host, which contributes to stabilizing Ni NPs in their metallic state. Ultimately, these properties could play a key role in activating H_2 *via* dissociation into H atoms irrespectively the feed composition, which then rapidly migrates to the NiO—CeO_{2-x} and NiO—La_2O_3 interfaces by the spillover effect [70].

Once CO_2 is adsorbed in form of carbonates, these species should be hydrogenated to methane on near Ni^0 sites (Fig. 7a and S10). The analysis of C1s region during the experiments under CO_2 methanation conditions (Fig. 7a) could also provide valuable information to link changes suffered by different actives sites and the reaction pathway during CO_2 methanation.

A variable peak can be observed at 293.1 eV for experiments with CO_2 in the inlet mixture, which is identified as gas-phase CO_2 [63,71]. As expected, the relative intensity of this peak decreases as long as temperature increases under CO_2 methanation mixture. Based on decreasing CO_2 signal ($m/z = 44$) monitored by mass spectroscopy during the NAP-XPS experiment under CO_2 methanation mixture (Fig. S9), this decrease can be ascribed to the promotion of CO_2 methanation reaction at increasing temperatures. In fact, an emerging peak for the gaseous methane can be identified at 288.1 eV as long as CO_2 gas peak decreases, whereas no peaks for CO gas can be observed between 291 and 292 eV, confirming the high selectivity of the catalyst [72].

At the same time, two peaks appear at 287.5 and 289.0 eV as long experiment temperature increases under CO_2 methanation mixture. Considering that almost all CO_3 are decomposed at a temperature above 350 ºC in the presence of CO_2 and H_2 gases, the peak at 289.0 eV cannot be assigned to CO_3* . In agreement with the reported in previous studies of the literature [64,71–78], the formation of formate (HCOO*) during CO_2 methanation could explain the presence of these peaks. Thus, formate specie (HCOO*) could act as the main reaction intermediate in the CO_2 to CH_4 conversion. Considering that the CO_3* peak intensity is reduced at increasing temperatures, simultaneously to the formation of HCOO* , the reduced CO_3* signal can be attributed to the conversion of CO_3* to HCOO* in the presence of hydrogen [79].

3.5. In situ NAP-XPS under a switching gas atmosphere at 300 °C

To analyse in detail if the catalyst's reduction or oxidation is predominant during the CO_2 methanation reaction, experiments under switching conditions were carried out at 300 °C (steps 3–5 in Fig. 1) with the previously analysed sample. Prior to the experiment, the sample was cooled from 450° to 150°C under the same CO_2 methanation mixture employed in step 2. Once the temperature was stabilized and steady-state was observed, only pure CO_2 was fed to the reaction chamber (step 3), and then the temperature was raised to 300 °C. After recording different repetitive spectra under pure CO_2, the inlet gas was switched consecutively to pure H_2 (step 4) and $CO_2 + H_2$ mixture (step 5). The inlet gas composition was maintained until the steady state was reached under each experimental condition. As previously described in step 2, three different incident energies (320, 375 and 1125 eV) were probed at each step to evaluate the effect of analysis depth on the nature of different species.

Fig. 8 shows the evolution of the Ni^0 (375 and 1225 eV) and Ce^{3+} (320 eV and 1125 eV) proportions at the steady state under different gas atmospheres analysed for the previously specified incident energies. These values were determined after deconvolution and integration of the XPS spectra included in Fig. S10. The resulting percentages of different species obtained from the spectra recorded after cooling the sample from 450 °C (step 2) to 150 °C under the CO_2 methanation mixture are also included with dotted lines as reference.

As can be observed, the oxidation state of Ni (Fig. 8a) and Ce (Fig. 8b) species is affected by CO_2 admission at 300 °C (step 3) and regional depth. On the one hand, the Ni^0 proportion decreases by 7% (1125 eV) and 8% (375 eV) with respect to reference conditions (dotted lines). This decrease denotes a noticeable oxidation of Ni^0 due to Ni^{2+}—CeO_{2-x} and/or Ni^{2+}—La_2O_3 interfaces formation, especially for those placed in more superficial layers. On the other hand, an oxidizing effect is also observed on the CeO_{2-x} support, resulting in a decrease in Ce^{3+} content with respect to reference conditions. Specifically, the Ce^{3+} proportion is 6% lower than those determined after step 2 for the 1125 and 320 eV photon energies. As exposure to CO_2 induces changes in the oxidation state of both Ce and Ni atoms, the reported results provide further evidence that both ceria and metallic Ni^0 contribute to the activation of CO_2, in line with the identification of an increasing carbonate signal near to 290.3 eV in the C1s region (Fig. 7b) [68,80,81].

In the step 4, the inlet gas was switched to pure H_2 at 300 °C. As can be observed, the Ni^0 and Ce^{3+} contents increase until exceeding the

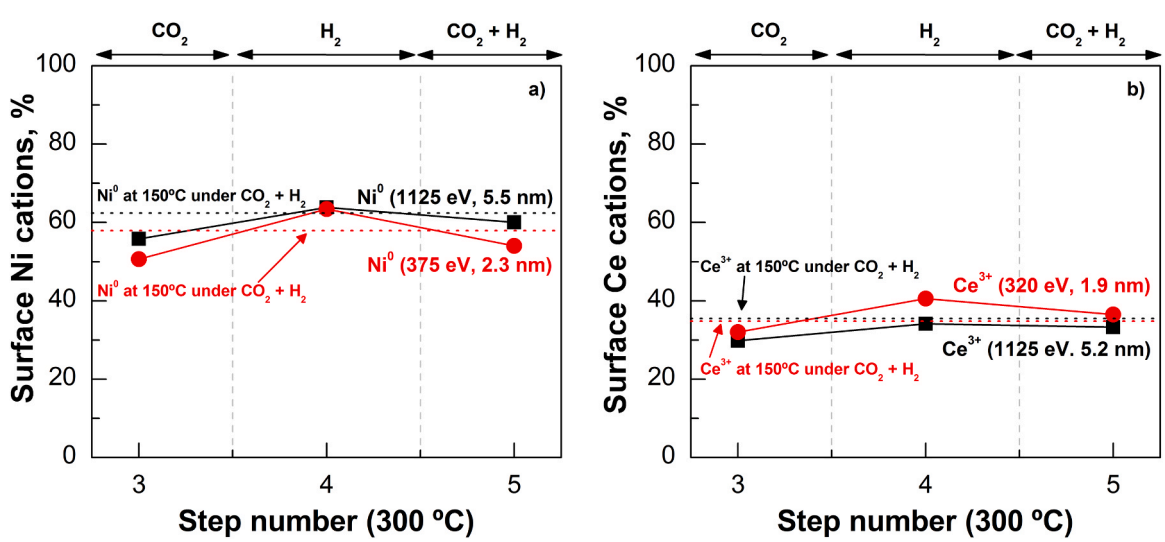

Fig. 8. Evolution of a) Ni^0 and b) Ce^{3+} contents relative to the total nickel and cerium contents, measured by NAP–XPS experiments under different feed compositions (CO_2, H_2 or $CO_2 + H_2$) (steps 3–5). The photon energies and probed depths (estimated as 3 times the inelastic mean free path, IMFP) are also indicated. Reference dotted lines indicate the initial content of different species recorded at 150 °C under the CO_2 methanation mixture (after cooling down from step 2).

values reported for both reference conditions (dotted lines). At the same time, the relative intensity of the carbonate and, especially formate group signals (Fig. 7b) decreases with respect to that observed for the experiment carried out under pure CO_2. This trend denotes that NiO and Ce^{4+} are easily reduced back by the addition of pure H_2 during this step, favouring the simultaneous hydrogenation of adsorbed CO_2. The lower stability of the HCOO* species observed after switching to pure H_2 again postulate them as more plausible intermediates for the CO_2 methanation reaction than the carbonate species [77,82].

The high reducibility of this novel material is among the most important factors that enhances the activation of the CO_2 methanation reaction at low temperatures. As expected, the reduction degree is higher for the species closer to the surface layers, especially in the case of NiO, in line with the higher reducibility observed in Fig. 5 for the perovskite phase with respect to the ceria support. The higher reactivity of the surface Ni NPs is assigned to the better contact with H_2 and/or CO_2, whereas Ni NPs in the inner layers show higher stability due to their insertion into the NiO—CeO_{2-x} interface.

Finally, the CO_2 methanation mixture was fed to the chamber (step 5). As observed in Fig. 8, both species are partially oxidized in the presence of CO_2 and H_2. Therefore, the Ni^0 (54% and 59% for the 375 and 1125 eV photon energies) and Ce^{3+} (36% and 33% for the 320 and 1125 eV photon energies) contents are intermediate to those reported in steps 3 and 4. This trend confirms that the surfaces of ceria and of nickel are oxidized on average during the CO_2 methanation reaction due to a faster CO_2 adsorption than H_2 chemisorption. However, no significant structural changes are expected on different phases during this process, except the decrease in the amount of oxygen vacancies in ceria support due to the dissociative adsorption of CO_2 on its surface.

3.6. *In situ FTIR experiments*

In situ FTIR experiments were performed with the aim of identifying the individual roles of Ni and Ce species as well as of the surface reaction intermediates under CO_2 adsorption and methanation conditions, which helps to establish CO_2 methanation pathways over the 10% $LaNiO_3$/CeO_2-derived catalyst. To facilitate the identification of the surface species on the spectra, the detailed assignment of the absorbance peaks detected during FTIR experiments under different operation conditions is summarized in Fig. 9.

Fig. 10 shows different FTIR spectra recorded during CO_2 adsorption at increasing temperatures for the prereduced (550 °C, 2 h) 10% $LaNiO_3$/CeO_2 sample. Immediately after exposure to the 5% CO_2/N_2 mixture at 150 °C (see black spectrum), three minor bands appear at 3468, 3632 and 3661 cm^{-1}, which follow different trends with increasing temperature. On the one hand, the bands at 3468 and 3661 cm^{-1} reach a maximum at 150 °C and then progressively decrease until becoming negative above 300 °C. As already described in the literature [62–64,83,84], these bands can be attributed to the vibration of bridged OH^- groups adsorbed onto the Ce^{3+} surface (Fig. S11a), and their disappearance implies the partial oxidation of Ce^{3+} to Ce^{4+}, in line with that observed in Fig. 6. On the other hand, although it follows a decreasing trend with increasing temperature, the tiny band identified at 3631 cm^{-1} is always positive. The bands centred at 1216 and 1423 cm^{-1} follow similar trends. Based on the literature [66,71,72], these positive bands correspond to OH^- vibration deformation (ν(OH)) or symmetric CO_3 stretching vibration ($\nu_s(CO_3)$) bands of surface mono- and bidentate bicarbonate species.

The opposite trends identified for OH^- groups and bicarbonates suggest that the later species could be formed by the reaction between CO_2 and weakly adsorbed oxygen on surface OH^- groups or surface oxygen species of the CeO_2 support [73–76]. In agreement with this assignment, the corresponding peaks are more intense for the bare CeO_2 support [83] (Fig. S11a). However, as long as the adsorption temperature increases, their decreasing intensity denotes that these species are not strongly attached to the ceria support, which is consistent with their desorption at low temperatures during CO_2-TPD experiments (Fig. S5). Alternatively, their conversion into other intermediates (such as mono- and bidentate carbonates or formates) could also contribute to this decreasing trend.

Regarding the 1700–900 cm^{-1} region, a broad signal composed of multiple bands can be identified. Notably, no negative bands appear at increasing temperatures, which discards the presence of characteristic bands of the OH^- groups of the CeO_2 support in this region. In contrast, wide and weak bands can be identified at 999, 1043, 1288, 1344 and 1552 cm^{-1} for all analysed temperature ranges.

Based on the CO_2-TPD (Fig. S5) and NAP-XPS results (Fig. 7), these bands can be assigned to $\nu_a(CO_2)$ and $\nu_s(CO_2)$ vibration modes of (chelating) mono-/bidentate carbonates mainly adsorbed on La_2O_3 sites and, to a minor extent, on the ceria support (Fig. S11a). These species could be formed due to the interaction of CO_2 with the basic surface of O_2^- species, which present medium-strong bond strength. Among them, the relative intensity of the bidentate carbonates bands (1000, 1288 and 1552 cm^{-1}) decreases in a higher extent than that of monodentate carbonates with increasing temperatures, denoting a lower stability of the former, which corresponds with our previous report [77].

In addition, small bands at 853, 1074 and 1469 cm^{-1} can be observed irrespective of the experimental temperature, which might be related to the formation of more stable organic compounds, such as polydentate carbonates [14,79,83]. Their stable nature could be related to the strong CO_2 adsorption on bulk-like La_2O_3 sites with high thermal stability (Fig. S5). The formation of a large variety of carbonate species on the surface of the 10% $LaNiO_3$/CeO_2-derived catalyst is beneficial for activating CO_2 molecules and, ultimately, enhancing CO_2 methanation.

Decreasing bands can be observed at 1373, 1389, 1592 and 2850 cm^{-1}, characteristic of the following vibration modes of mono- and bidentate formates: symmetric OCO stretching ($\nu_s(CO_2)$), CH deformation (δ(CH)), asymmetric OCO stretching ($\nu_{as}(CO_2)$) and CH deformation (ν(CH)), respectively [62,79,84]. The formation of $HCOO^-$ is ascribed to the hydrogenation of adsorbed CO_2 (in the form of

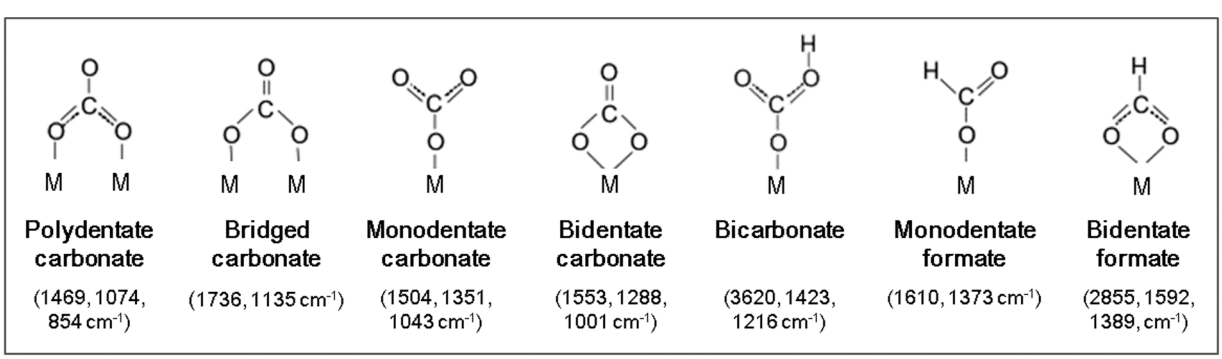

Fig. 9. Scheme of surface carbon species and reported adsorption regions in infrared spectra.

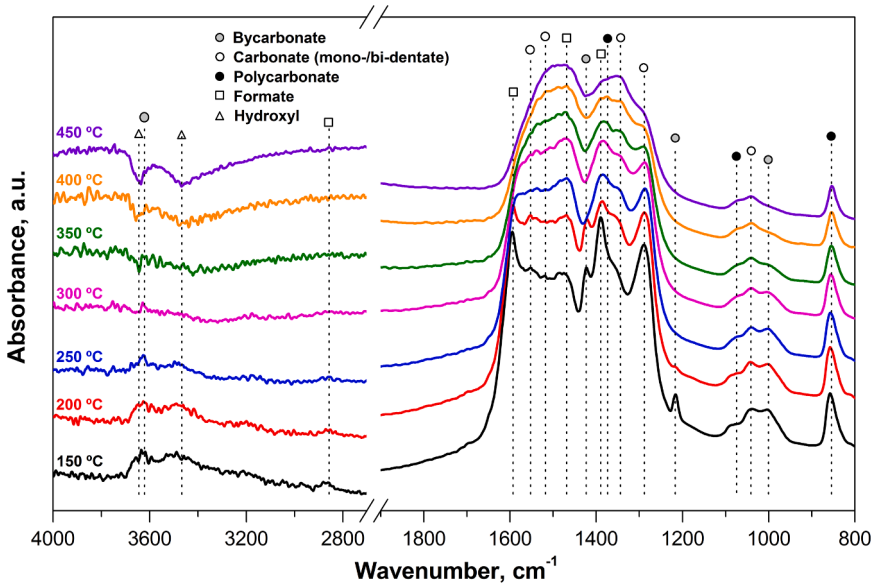

Fig. 10. *In situ* FTIR spectra for the prereduced 10% $LaNiO_3/CeO_2$ sample during CO_2 adsorption at different temperatures. Spectra were recorded after 30 min of exposure to a CO_2/N_2 mixture.

carbonates or bicarbonates) with residual H_2, which is previously chemisorbed on Ni^0 sites during the prereduction step *via* a spillover process, or with the hydroxyl groups formed on ceria [85]. Thus, these peaks start to decrease as long as the residual adsorbed hydrogen is consumed. However, their formation by the subsequent reaction of the adsorbed CO, identified for the bare CeO_2 support (Fig. S11a), with OH^- groups ($CO^* + OH^* \rightarrow HCOO^*$) cannot be discarded [70]. Finally, the intense double band of gas phase CO_2 is also noticed at approximately 2350 cm^{-1} (not shown), irrespective of the reaction temperature [77].

After studying CO_2 adsorption over the 10% $LaNiO_3/CeO_2$-derived sample, CO_2 methanation was analysed by performing *in situ* FTIR experiments after exposure of the sample to a 0.1% CO_2:0.4% H_2:99.5% N_2 mixture for 30 min in the 150–450 °C temperature range (Fig. 11).

Some differences can be identified with respect to the previously recorded spectra under CO_2 adsorption conditions. On the one hand, no clear bands can be observed in the 3400–3700 cm^{-1} region, which is derived from the low stability or rapid transformation of adsorbed bicarbonates on the ceria support under CO_2 methanation conditions. Furthermore, the absence of bands in this region could be supported by the partial adsorption of H_2O, which is generated due to the Sabatier reaction, in the form of hydroxyls as well as the partial oxidation of the ceria support [73,83]. On the other hand, the intensity of the bands previously ascribed to mono- and bidentate carbonates (1001, 1043, 1288, 1351, 1504 and 1553 cm^{-1}) decreased under CO_2 methanation conditions. Regardless, even in the presence of hydrogen, their identification suggests a higher stability of carbonates (especially monocarbonates) than bicarbonates during the CO_2 methanation reaction [72, 79]. Note that the $La_2O_2CO_3$ phase was identified in the XRD diffractogram performed on the used sample after the CO_2 methanation reaction (Fig. S1), and the characteristic peaks of carbonates (290.2 eV) were identified in the spectra recorded in the C1s region under the CO_2 methanation mixture (Fig. 7). This knowledge further confirms their

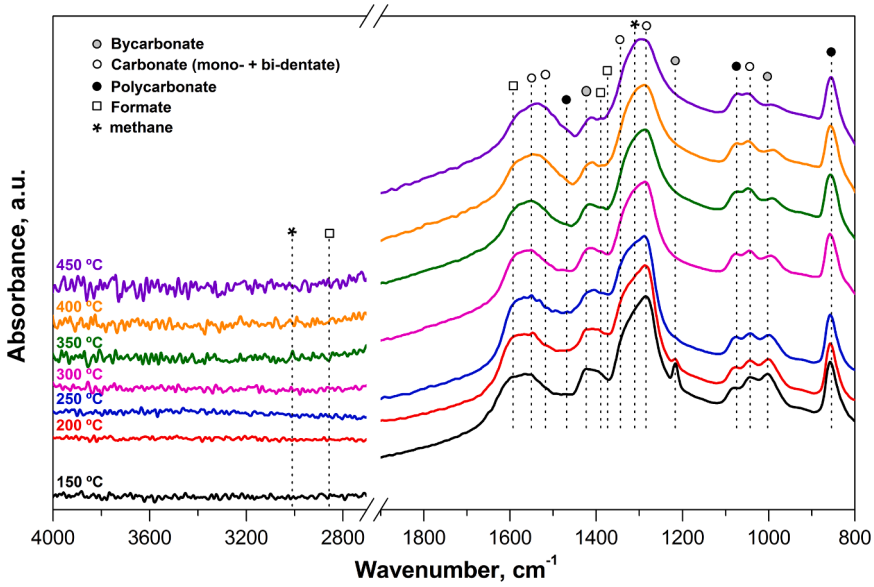

Fig. 11. *In situ* FTIR spectra for the prereduced 10% $LaNiO_3/CeO_2$ sample during CO_2 methanation at different temperatures. Spectra were recorded after 30 min of exposure to a CO_2/He mixture.

stable behaviour during the CO_2 methanation reaction.

In contrast, the intensity of the characteristic bands of the formate species (1373, 1389 and 1592 cm^{-1}) increases with respect to that observed in the spectra collected during CO_2 adsorption (Fig. 10). This trend is in line with the identification of weak peaks at 287.5 and 289.4 eV in the C 1 s region under CO_2 methanation conditions (Fig. 7a) at increasing temperatures due to formate formation, and suggests that the inclusion of H_2 in the feed stream favours the hydrogenation of the adsorbed CO_2 to formates. As a result, the bands of mono- and, especially, bidentate carbonates simultaneously decrease. In contrast, polydentate carbonates slightly increase with the experimental temperature, so their role as spectators is probable due to their high stability. This trend is in line with the identification of carbonates peaks in the C1s region at high temperatures under CO_2 methanation conditions (Fig. 7a).

Our results indicate that part of the CO_2 adsorbed species in the form of bicarbonates and carbonates are converted into formate due to the reaction with the hydrogen atoms resulting from H_2 dissociation at low and medium-high temperatures, respectively [76,85]. However, formate formation from the reaction of adsorbed CO* with OH^- groups of ceria cannot be ruled out since the characteristic bands of CO adsorbed on Ce^{3+} (2149 cm^{-1}) and Ce^{4+} (2184 cm^{-1}) sites are identified for the ceria support in Fig. S11 [70]. Regardless, this process should be minor or too fast for a fully formulated sample since no bands were verified in the carbonyl region (1800–2100 cm^{-1}) under our experimental conditions. Thus, it can be assumed that this compound is not formed on Ni^0 sites due to CO_2 disproportionation [66,82], in line with the high selectivity towards methane (> 95%) obtained during activity tests (Fig. 1) and the high Ni^0 proportion identified by NAP-XPS under CO_2 methanation conditions (Fig. 6). In contrast, an increasing shoulder on the left side (≈ 1310 cm^{-1}) of the band centred at 1286 cm^{-1} and a small peak at 3013 cm^{-1} can be observed at increasing temperatures. Based on previous studies [42,62,75,86], these new increasing bands are ascribed to the C—H bending (δ(CH)) and stretching (ν(CH)) vibration modes of gaseous CH_4, formed due to the occurrence of the CO_2 methanation reaction. The occurrence of the Sabatier reaction can be further verified by the appearance of a shoulder on the left side of the peak at 1592 cm^{-1} (≈ 1655 cm^{-1}), which is ascribed to surface-bound water [86].

Thus, it can be concluded that formates instead of carbonyls are involved in the CO_2 methanation reaction over this novel catalyst. As a result, the formate species can be considered as the main reaction intermediates during CO_2 methanation over 10% $LaNiO_3/CeO_2$-derived catalysts.

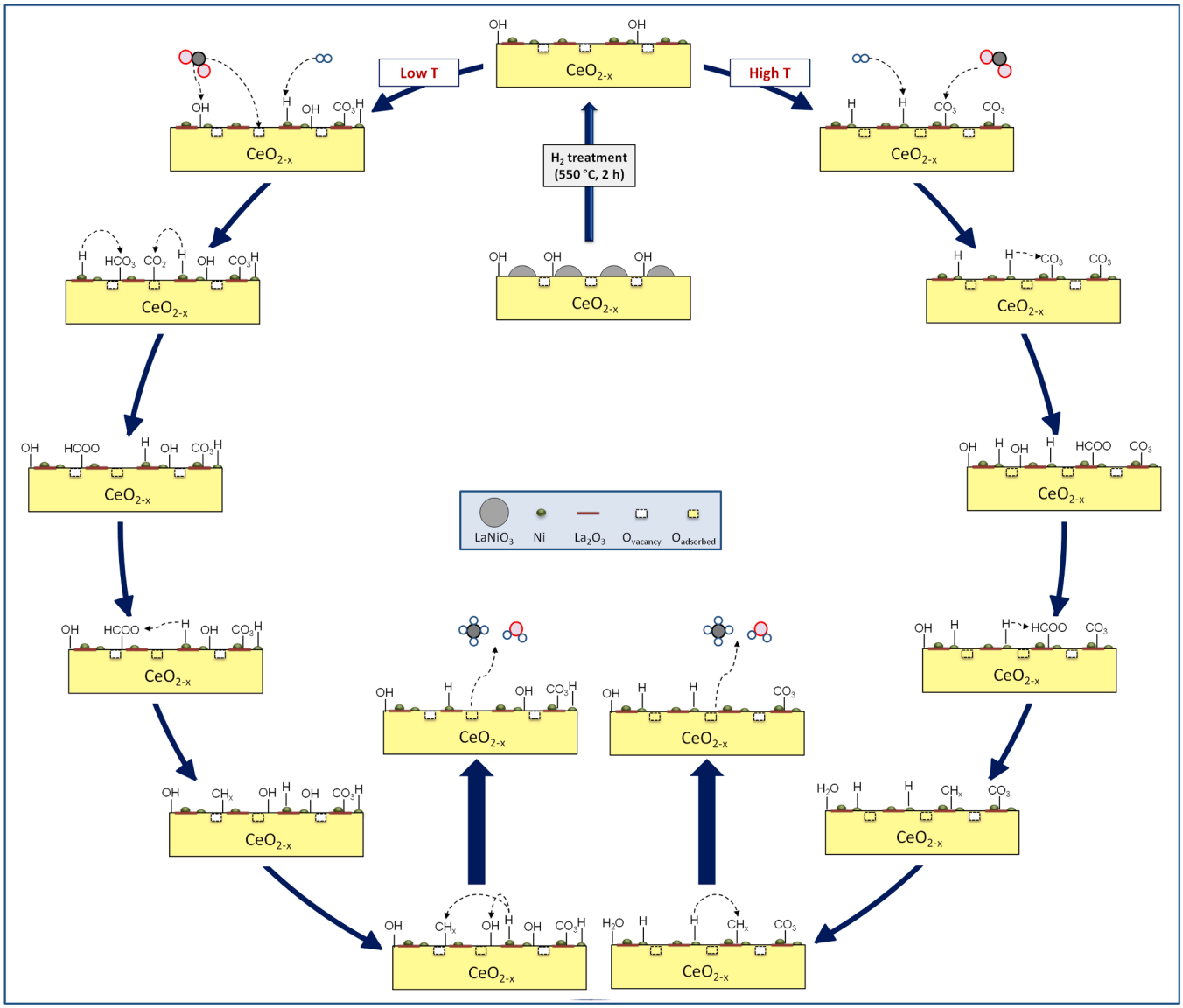

Fig. 12. Schematic illustration of proposed CO_2 methanation mechanism and the role of different active sites.

3.7. CO_2 methanation mechanism

Combining *in situ* FTIR and NAPS-XPS experiments, it can be deduced the essential reaction mechanism for the CO_2 methanation reaction on the 10% $LaNiO_3/CeO_2$-derived catalyst and the behaviour and changes suffered by the different active sites under reaction conditions. As can be observed in Fig. 12, after the *in situ* reduction of 10% $LaNiO_3/CeO_2$ precursor, a mix between finely dispersed Ni^0 nanoparticles (≈1.5 nm) and Ni^{2+}—CeO_{2-x} and Ni^{2+}—La_2O_3 mixed oxides was formed.

Once the desired catalyst was obtained from 10% $LaNiO_3/CeO_2$ precursor, CO_2 methanation experiments were performed. As observed, CeO_{2-x} can efficiently adsorb CO_2 at low temperatures, in the form of bicarbonates (HCO_3*), with the participation of oxygen vacancies and hydroxyl groups (OH^-) or leading to a progressive oxidation of its surface. As long as temperature increase and ceria support is reoxidated, CO_2 adsorption on La_2O_3 sites, in the form of mono-/bi-/polydentate carbonates (CO_3*), becomes predominant. Meanwhile, Ni^0 nanoparticles are mainly related with H_2 adsorption and dissociation. It is worth to mention that the metallic Ni^0 proportion is high during whole temperature range, limiting Ni-carbonyls formation and confirming that a high concentration of active sites is available for CO_2 hydrogenation even at high temperatures. Then, the H_2 dissociated on Ni^0 sites reacts progressively with bicarbonates, bidentate carbonates and modentate carbonates on near basic sites at increasing temperatures, leading to formate (HCOO*) formation as the main reaction intermediate. In contrast, polydentate carbonates act as spectator during this process. Finally, formate species are rapidly hydrogenated into CH_4 with the atomic H dissociated in highly dispersed Ni^0 sites. The low amount of CO formed due to CO_2 dissociation on ceria surface (Figs. S6 and S11a) could be easily hydrogenated on near Ni^0 sites since no CO species are detected during *in situ* FTIR and NAP-XPS experiments.

The high activity, selectivity and stability of this catalyst could be ascribed to a high amount of metallic nickel nanoparticles for H_2 dissociation, even under CO_2 methanation conditions at high temperature, the presence of different nature basic sites for CO_2 adsorption and the strong interaction between different phases, which favours H transfer and prevent them from agglomeration.

4. Conclusions

The 10% $LaNiO_3/CeO_2$-derived catalyst emerges as promising alternative for the CO_2 methanation reaction. The reaction mechanism and the role of different active sites during the CO_2 methanation have been explored during the CO_2 methanation reaction by *in situ* NAP-XPS and FTIR experiments.

In situ NAP-XPS experiments and the main physico-chemical properties confirm the reduction of Ni-based species and CeO_{2-x} during reduction step (500 ºC), leading to the conformation of small Ni^0 nanoparticles and Ni^{2+}—CeO_{2-x} and Ni^{2+}—La_2O_3 mixed oxides in intimate contact. During CO_2 methanation, a progressive reoxidation of Ni^0 and Ce^{3+} is observed, especially at the surface, indicating that CO_2 adsorption is faster than dissociative H_2 chemisorption. This phenomenon is ascribed to the participation of oxygen vacancies of the ceria support in the CO_2 adsorption mechanism and to the partial accommodation of Ni on the NiO—CeO_{2-x} and NiO—La_2O_3 interfaces, which favours the O* transfer from CeO_{2-x} and La_2O_3 in close contact with Ni. Regardless, the Ni^0 content is significantly higher (64%−51%) than that observed for the conventional Ni/CeO_2 catalyst (> 50%). This property favours H_2 activation *via* dissociation into H atoms, which then can rapidly hydrogenate the CO_2 adsorbed on NiO—CeO_{2-x} and NiO—La_2O_3 interfaces due to the spillover effect.

In situ FTIR experiments combined with the analysis of C1s region (NAP-XPS) suggest that the reaction pathway begins with the CO_2 is associative chemisorption (CO_2* or CO_3*) on hydroxyl groups, oxygen vacancies and surface oxygen of ceria and, then, follows which CO_2 adsorption on La_2O_3 sites, in the form of bicarbonates as well as mono-, bi- and polydentate carbonates at increasing temperatures. Finally, bicarbonates as well as bi- and monodentate carbonates react progressively at increasing temperatures with the hydrogen atoms spilled over from Ni^0 nanoparticles to produce formates as the main reaction intermediates, which are rapidly hydrogenated to methane.

In short, the formation of a large variety of carbonate species on the surface of the 10% $LaNiO_3/CeO_2$-derived catalyst is beneficial for activating CO_2 molecules, whereas the high proportion and dispersion of Ni^0 NPs favour H_2 dissociation and transfer. Both factors together with the intimate contact between different phases enhance CO_2 methanation efficiency and stability with respect to previously reported perovskite-derived catalysts.

CRediT authorship contribution statement

Jon A. Onrubia-Calvo: Validation, Methodology, Visualization, Writing – original draft. **Sergio López-Rodríguez:** Validation, Methodology, Visualization, Investigation, Writing – review & editing. **Ignacio J. Villar-García:** Investigation – ALBA technical support & experimentation. Writing – review & editing. **Virginia Pérez-Dieste:** Investigation – ALBA technical support & experimentation. Writing – review & editing. **Agustín Bueno-López:** Conceptualization, Supervision, Project administration, Funding acquisition, Writing – review & editing. **Juan R. González-Velasco:** Conceptualization, Supervision, Project administration, Funding acquisition, Writing – review & editing.

Declaration of Competing Interest

The authors declare that they have no known competing financial interests or personal relationships that could have appeared to influence the work reported in this paper.

Data availability

Data will be made available on request.

Acknowledgements

Support for this study was provided by Projects PID2019–105960RB-C21 and PID2019–105960RB-C22 by MCIN/AEI/10.13039/501100011033, the Basque Government (Project IT1509–2022), Generalitat Valenciana (CIPROM/2021/74) and ALBA synchrotron. One of the authors (JAOC) acknowledges the postdoctoral research grant (DOCREC20/49) provided by the University of the Basque Country (UPV/EHU).

Supporting information

Supporting information includes detailed information about the main physico-chemical properties of fresh and used 10% $LaNiO_3/CeO_2$ sample, *i.e.*, XRD diffractograms (Fig. S1), N_2 adsorption-desorption isotherms (Fig. S2), STEM-EDS images (Fig. S3), temperature programmed desorption of H_2 (H_2-TPD, Fig. S4) and CO_2 (CO_2-TPD, Fig. S5) profiles as well as the main textural properties (Table S1), different basic site concentrations (Table S2) and surface species properties (XPS, Table S3). The catalytic activity of bulk perovskite ($LaNiO_3$) and ceria support (CeO_2) is also included as reference. Ni 3p andCe 3d spectra recorded during *in situ* NAP-XPS experiments (Fig. S6) under different reaction conditions (Figs. S7-S8 and S10) at different energies (Table S4) as well as the CO_2 signal ($m/z = 44$) monitored during the NAP-XPS experiment under the CO_2 methanation mixture (Fig. S9) are also included. Meanwhile, *in situ* FTIR spectra for pre-reduced CeO_2 sample during CO_2 adsorption and CO_2 methanation at increasing temperatures is also included as reference (Fig. S11).

Appendix A. Supporting information

Supplementary data associated with this article can be found in the online version at doi:10.1016/j.apcatb.2023.123367.

References

[1] S. Sun, H. Sun, P.T. Williams, C. Wu, Recent advances in integrated CO_2 capture and utilization: a review, Sust. Energy Fuels 5 (2021) 4546–4559.

[2] European Commission. Energy Roadmap 2050 (2011). ⟨https://ec.europa.eu/energy/sites/ener/files/documents/2012_energy_roadmap_2050_en_0.pdf⟩ (accessed October, 2020) (2011).

[3] Z. Sverko Grdic, M. Krstinic Nizic, E. Rudan, Circular economy concept in the context of economic development in EU countries, Sustainability 12 (2020) 3060–3073.

[4] N. Wang, Z. Guo, F. Meng, H. Wang, J. Yin, Y. Liu, The circular economy and carbon footprint: a systematic accounting for typical coal-fuelled power industrial parks, J. Clean. Prod. 229 (2019) 1262–1273.

[5] P. Sabatier, New synthesis of methane, Comptes Rendus 134 (1902) 514–516.

[6] S. Schiebahn, T. Grube, M. Robinius, V. Tietze, B. Kumar, D. Stolten, Power to gas: technological overview, systems analysis and economic assessment for a case study in Germany, Int. J. Hydrog. Energy 40 (2015) 4285–4294.

[7] M. Götz, J. Lefebvre, F. Mörs, A. McDaniel Koch, F. Graf, S. Bajohr, R. Reimert, T. Kolb, Renewable power-to-gas: a technological and economic review, Renew. Energ. 85 (2016) 1371–1390.

[8] I.A. Gondal, Offshore renewable energy resources and their potential in a green hydrogen supply chain through power-to-gas, Sustain, Energy Fuels 3 (2019) 1468–1489.

[9] A. Quindimil, U. De-La-Torre, B. Pereda-Ayo, A. Davó-Quiñonero, E. Bailón-García, D. Lozano-Castelló, J.A. González-Marcos, A. Bueno-López, J.R. González-Velasco, Effect of metal loading on the CO_2 methanation: a comparison between alumina supported Ni and Ru catalysts, Catal. Today 356 (2019) 419–432.

[10] A. Bermejo-López, B. Pereda-Ayo, J.A. González-Marcos, J.R. González-Velasco, Ni loading effects on dual function materials for capture and in-situ conversion of CO_2 to CH_4 using CaO or Na_2CO_3, J. CO_2 Util. 34 (2019) 576–587.

[11] L. Dai, X. Lu, G. Chu, C. He, W. Zhan, G. Zhou, Surface tuning of $LaCoO_3$ perovskite by acid etching to enhance its catalytic performance, Rare Met. 40 (2021) 555–562.

[12] Y. Nishihata, J. Mizuki, T. Akao, H. Tanaka, M. Uenishi, M. Kimura, T. Okamoto, N. Hamada, Self-regeneration of a Pd-perovskite catalyst for automotive emissions control, Nature 418 (2002) 164–167.

[13] J. Gao, Li-shan Jia, Wei-ping Fang, Qing-biao Li, H. Song, Methanation of carbon dioxide over the $LaNiO_3$ perovskite catalysts activated under the reactant stream, J. Fuel Chem. Technol. 37 (2009) 573–577.

[14] P.A.U. Aldana, F. Ocampo, K. Kobl, B. Louis, F. Thibault-Starzyk, M. Daturi, P. Bazin, S. Thomas, A.C. Roger, Catalytic CO_2 valorization into CH_4 on Ni-based ceria-zirconia. Reaction mechanism by operando IR spectroscopy, Catal. Today 215 (2013) 201–207.

[15] Q. Pan, J. Peng, T. Sun, S. Wang, S. Wang, Insight into the reaction route of CO_2 methanation: promotion effect of medium basic sites, Catal. Commun. 45 (2014) 74–78.

[16] S. Tada, T. Shimizu, H. Kameyama, T. Haneda, R. Kikuchi, Ni/CeO_2 catalysts with high CO_2 methanation activity and high CH_4 selectivity at low temperatures, Int. J. Hydrog. Energy 37 (2012) 5527–5531.

[17] V. Alcalde-Santiago, A. Davó-Quiñonero, D. Lozano-Castelló, A. Quindimil, U. De-La-Torre, B. Pereda-Ayo, J.A. González-Marcos, J.R. González-Velasco, A. Bueno-López, Ni/LnOx catalysts (Ln⁻La, Ce or Pr) for CO_2 methanation, ChemCatChem 11 (2019) 810–819.

[18] P. Frontera, A. Macario, M. Ferraro, P. Antonucci, Supported catalysts for CO_2 methanation: a review, Catalysts 7 (2017) 59–87.

[19] Z. Li, T. Zhao, L. Zhang, Promotion effect of additive Fe on Al2O3 supported Ni catalyst for CO_2 methanation, Appl. Organo Chem. 32 (2018), e4328.

[20] J. Lin, C. Ma, J. Luo, X. Kong, Y. Xu, G. Ma, J. Wang, C. Zhang, Z. Li, M. Ding, Preparation of Ni based mesoporous Al_2O_3 catalyst with enhanced CO_2 methanation performance, RSC Adv. 9 (2019) 8684–8694.

[21] Z. Zhang, Y. Tian, L. Zhang, S. Hu, J. Xiang, Y. Wang, L. Xu, Q. Liu, S. Zhang, X. Hu, Impacts of nickel loading on properties, catalytic behaviors of Ni/γ–Al_2O_3 catalysts and the reaction intermediates formed in methanation of CO_2, Int. J. Hydrog. Energy 44 (2019) 9291–9306.

[22] Y. Zhan, Y. Wang, D. Gu, C. Chen, L. Jiang, K. Takehira, Ni/Al_2O_3-ZrO_2 catalyst for CO_2 methanation: the role of γ-(Al, Zr)2O3 formation, Appl. Surf. Sci. 459 (2018) 74–79.

[23] J.A. Onrubia-Calvo, B. Pereda-Ayo, J.A. González-Marcos, A. Bueno-López, J. R. González-Velasco, Design of CeO_2-supported $LaNiO_3$ perovskites as precursors of highly active catalysts for CO_2 methanation, Catal. Sci. Technol. 11 (2021) 6065–6079.

[24] P. Steiger, R. Delmelle, D. Foppiano, L. Holzer, A. Heel, M. Nachtegaal, O. Kröcher, D. Ferri, Structural reversibility and nickel particle stability in lanthanum iron nickel perovskite-type catalysts, ChemSusChem 10 (2017) 2505–2517.

[25] K. Wang, W. Li, J. Huang, J. Huang, G. Zhan, Q. Li, Enhanced active site extraction from perovskite $LaCoO_3$ using encapsulated PdO for efficient CO_2 methanation, J. Energy Chem. 53 (2021) 9–19.

[26] J. Ren, C. Mebrahtu, L. van Koppen, F. Martinovic, J.P. Hofmann, E.J.M. Hensen, R. Palkovits, Enhanced CO_2 methanation activity over $La_{2-x}Ce_xNiO_4$ perovskite-derived catalysts: Understanding the structure-performance relationships, Chem. Eng. J. 426 (2021), 131760.

[27] C. Dong, H. Sun, Y. Zhou, H. Zhan, G. Wang, W. Liu, S. Bi, B. Ma, Transition metal (Ni, Cu, Ga, Fe) doped $LaCoO_3$ improve surface hydrogen activation to promote low-temperature CO_2 methanation, J. Environ. Chem. Eng. 10 (2022), 107718.

[28] H.S. Lim, G. Kim, Y. Kim, M. Lee, D. Kang, H. Lee, J.W. Lee, Ni-exsolved $La_{1-x}Ca_xNiO_3$ perovskites for improving CO_2 methanation, Chem. Eng. J. 412 (2021), 127557.

[29] C. Tsounis, Y. Wang, H. Arandiyan, R.J. Wong, C.Y. Toe, R. Amal, J. Scott, Tuning the selectivity of $LaNiO_3$ perovskites for CO_2 hydrogenation through potassium substitution, Catalysts 10 (2020) 409–425.

[30] H. Arandiyan, Y. Wang, J. Scott, S. Mesgari, H. Dai, R. Amal, In situ exsolution of bimetallic Rh-Ni nanoalloys: a highly efficient catalyst for CO_2 methanation, ACS Appl. Mater. Interfaces 10 (2018) 16352–16357.

[31] J. Zhang, B. Ren, G. Fan, L. Yang, F. Li, Exceptional low-temperature activity of a perovskite-type $AlCeO_3$ solid solution-supported Ni-based nanocatalyst towards CO_2 methanation, Catal. Sci. Technol. 11 (2021) 3894–3904.

[32] A. Blanco, J. Caroca, R. Tamayo, M. Flores, M. Romero-Sáez, R. Espinoza-González, F. Gracia, CO_2 methanation activity of Ni-doped perovskites, Fuel 320 (2022), 123954.

[33] X. Wang, L. Zhu, Y. Zhuo, Y. Zhu, S. Wang, Enhancement of CO_2 methanation over La-modified Ni/SBA-15 catalysts prepared by different doping methods, ACS Sustain. Chem. Eng. 7 (2019) 14647–14660.

[34] T. Zhang, Q. Liu, Perovskite $LaNiO_3$ nanocrystals inside mesostructured cellular foam silica: high catalytic activity and stability for CO_2 methanation, Energy Technol. 8 (2020) 1901164.

[35] S. Li, S. Guo, D. Gong, N. Kang, K. Fang, Y. Liu, Nano composite composed of MoO_x-La_2O_3Ni on SiO_2 for storing hydrogen into CH_4 via CO_2 methanation, Int. J. Hydrog. Energy 44 (2019) 1597–1609.

[36] T. Zhang, Q. Liu, Mesostructured cellular foam silica supported bimetallic $LaNi_{1-x}Co_xO_3$ catalyst for CO_2 methanation, Int. J. Hydrog. Energy 45 (2020) 4417–4426.

[37] J.Y. Do, N. Park, M.W. Seo, D. Lee, H. Ryu, M. Kang, Effective thermocatalytic carbon dioxide methanation on Ca-inserted NiTiO3 perovskite, Fuel 271 (2020), 117624.

[38] S. Li, G. Liu, S. Zhang, K. An, Z. Ma, L. Wang, Y. Liu, Cerium-modified Ni-La_2O_3/ZrO_2 for CO_2 methanation, J. Energy Chem. 43 (2020) 155–164.

[39] M. Salmeron, R. Schlögl, Ambient pressure photoelectron spectroscopy: a new tool for surface science and nanotechnology, Surf. Sci. Rep. 63 (2008) 169–199.

[40] S. López-Rodríguez, A. Davó-Quiñonero, E. Bailón-García, D. Lozano-Castelló, F. C. Herrera, E. Pellegrin, C. Escudero, M. García-Melchor, A. Bueno-López, Elucidating the role of the metal catalyst and oxide support in the Ru/CeO_2-Catalyzed CO_2 methanation mechanism, J. Phys. Chem. C. 125 (2021) 25533–25544.

[41] S. López-Rodríguez, A. Davó-Quiñonero, E. Bailón-García, D. Lozano-Castelló, I. J. Villar-Garcia, V.P. Dieste, J.A. Onrubia-Calvo, J.R. González-Velasco, A. Bueno-López, Monitoring by in situ NAP-XPS of active sites for CO_2 methanation on a Ni/CeO_2 catalyst, J. CO_2 Util. 60 (2022), 101980.

[42] A. Quindimil, M.C. Bacariza, J.A. González-Marcos, C. Henriques, J.R. González-Velasco, Enhancing the CO_2 methanation activity of γ-Al_2O_3 supported mono- and bi-metallic catalysts prepared by glycerol assisted impregnation, Appl. Catal. B: Environ. 296 (2021), 120322.

[43] X. Lian, J. Gao, Y. Ding, Y. Liu, W. Chen, Unraveling catalytic reaction mechanism by in situ near ambient pressure x-ray photoelectron spectroscopy, J. Phys. Chem. Lett. 13 (2022) 8264–8277.

[44] S. Tanuma, C.J. Powell, D.R. Penn, Calculations of electron inelastic mean free paths. V. Data for 14 organic compounds over the 50–2000 eV range, Surf. Interface Anal. 21 (1994) 165–176.

[45] M.A.A. Aziz, A.A. Jalil, S. Triwahyono, A. Ahmad, CO_2 methanation over heterogeneous catalysts: recent progress and future prospects, Green. Chem. 17 (2015) 2647–2663.

[46] J.H. Kwak, L. Kovarik, J. Szanyi, Heterogeneous catalysis on atomically dispersed supported metals: CO_2 reduction on multifunctional Pd catalysts, ACS Catal. 3 (2013) 2094–2100.

[47] Y. Liu, S. Wang, Y. Hsu, H. Kai, P. Jasinski, Characteristics of $LaCo_{0.4}Ni_{0.6-x}Cu_xO_{3-\delta}$ ceramics as a cathode material for intermediate-temperature solid oxide fuel cells, J. Eur. Ceram. Soc. 38 (2018) 1654–1662.

[48] L. Qiao, X. Bi, Direct observation of Ni^{3+} and Ni^{2+} in correlated $LaNiO_{3-\delta}$ films, EPL (Europhys. Lett.) 93 (2011) 57002.

[49] Moulder J.F., Stickle W.F., Sobol P.E. and Bomben K.D., Handbook of X-ray Photoelectron Spectroscopy, Perkin-Elmber Corporation, Minnesota, 1992.

[50] R. Clauberg, W. Gudat, E. Kisker, E. Kuhlmann, G.M. Rothberg, Nature of the resonant 6-eV satellite in Ni: photoelectron spin-polarization analysis, Phys. Rev. Lett. 47 (1981) 1314–1317.

[51] L. Pino, A. Vita, M. Laganà, V. Recupero, Hydrogen from biogas: catalytic tri-reforming process with Ni/LaCeO mixed oxides, Appl. Catal. B: Environ. 148–149 (2014) 91–105.

[52] W. Zhong, T. Jiang, Y. Dang, J. He, S. Chen, C. Kuo, D. Kriz, Y. Meng, A. G. Meguerdichian, S.L. Suib, Mechanism studies on methyl orange dye degradation by perovskite-type LaNiO3-δ under dark ambient conditions, Appl. Catal. A: Gen. 549 (2018) 302–309.

[53] J. El Fallah, L. Hilaire, M. Roméo, F. Le Normand, Effect of surface treatments, photon and electron impacts on the ceria 3d core level, J. Electron Spectros Relat. Phenom. 73 (1995) 89–103.

[54] F. Le Normand, J. El Fallah, L. Hilaire, P. Légaré, A. Kotani, J.C. Parlebas, Photoemission on 3d core levels of cerium: an experimental and theoretical

investigation of the reduction of cerium dioxide, Solid State Commun. 71 (1989) 885–889.
[55] A. Pfau, K.D. Schierbaum, The electronic structure of stoichiometric and reduced CeO_2 surfaces: an XPS, UPS and HREELS study, Surf. Sci. 321 (1994) 71–80.
[56] J. Onrubia-Calvo, B. Pereda-Ayo, J.A. González-Marcos, A. Bueno-López, J. R. González-Velasco, Design of CeO_2-supported $LaNiO_3$ perovskites as precursors of highly active catalysts for CO_2 methanation, Catal. Sci. Technol. 11 (2021) 6065–6079.
[57] A. Arranz, C. Palacio, Interaction of Ni/Al interfaces with oxygen, Langmuir 18 (2002) 1695–1701.
[58] T. Maneerung, K. Hidajat, S. Kawi, K-doped $LaNiO_3$ perovskite for high-temperature water-gas shift of reformate gas: Role of potassium on suppressing methanation, Int. J. Hydrog. Energy 42 (2017) 9840–9857.
[59] S. Singh, D. Zubenko, B.A. Rosen, Influence of $LaNiO_3$ shape on its solid-phase crystallization into coke-free reforming catalysts, ACS Catal. 6 (2016) 4199–4205.
[60] A. Cárdenas-Arenas, A. Quindimil, A. Davó-Quiñonero, E. Bailón-García, D. Lozano-Castelló, U. De-La-Torre, B. Pereda-Ayo, J.A. González-Marcos, J. R. González-Velasco, A. Bueno-López, Design of active sites in Ni/CeO_2 catalysts for the methanation of CO_2: tailoring the Ni-CeO_2 contact, Appl. Mater. Today 19 (2020), 100591.
[61] E.- Yang, N.Y. Kim, G. Choi, S.S. Lim, D.J. Moon, Steam CO_2 reforming of methane over $La_{1-x}Ce_xNiO_3$ perovskite catalysts, Int. J. Hydrog. Energy 40 (2015) 11831–11839.
[62] J. Ashok, M.L. Ang, S. Kawi, Enhanced activity of CO_2 methanation over Ni/CeO_2-ZrO_2 catalysts: influence of preparation methods, Catal. Today 281 (2017) 304–311.
[63] Y. Yu, Y.M. Chan, Z. Bian, F. Song, J. Wang, Q. Zhong, S. Kawi, Enhanced performance and selectivity of CO_2 methanation over g-C_3N_4 assisted synthesis of $NiCeO_2$ catalyst: kinetics and DRIFTS studies, Int. J. Hydrog. Energy 43 (2018) 15191–15204.
[64] Y. Guo, S. Mei, K. Yuan, D. Wang, H. Liu, C. Yan, Y. Zhang, Low-temperature CO_2 methanation over CeO_2-supported Ru single atoms, nanoclusters, and nanoparticles competitively tuned by strong metal–support interactions and H-spillover effect, ACS Catal. 8 (2018) 6203–6215.
[65] A. Bueno-López, K. Krishna, M. Makkee, Oxygen exchange mechanism between isotopic CO_2 and Pt/CeO_2, Appl. Catal. A: Gen. 342 (2008) 144–149.
[66] A. Solis-Garcia, J.F. Louvier-Hernandez, A. Almendarez-Camarillo, J.C. Fierro-Gonzalez, Participation of surface bicarbonate, formate and methoxy species in the carbon dioxide methanation catalyzed by ZrO_2-supported Ni, Appl. Catal. B: Environ. 218 (2017) 611–620.
[67] L. Lin, S. Yao, Z. Liu, F. Zhang, N. Li, D. Vovchok, A. Martínez-Arias, R. Castañeda, J. Lin, S.D. Senanayake, D. Su, D. Ma, J.A. Rodriguez, In situ characterization of Cu/CeO_2 nanocatalysts for CO_2 hydrogenation: morphological effects of nanostructured ceria on the catalytic activity, J. Phys. Chem. C. 122 (2018) 12934–12943.
[68] Z. Liu, D.C. Grinter, P.G. Lustemberg, T. Nguyen-Phan, Y. Zhou, S. Luo, I. Waluyo, E.J. Crumlin, D.J. Stacchiola, J. Zhou, J. Carrasco, H.F. Busnengo, M. Ganduglia-Pirovano, S.D. Senanayake, J.A. Rodriguez, Dry reforming of methane on a highly-active Ni-CeO_2 catalyst: effects of metal-support interactions on C−H bond breaking, Angew. Chem. Int. Ed. 55 (2016) 7455–7459.
[69] J.A. Onrubia-Calvo, A. Bermejo-López, S. Pérez-Vázquez, B. Pereda-Ayo, J. A. González-Marcos, J.R. González-Velasco, Applicability of $LaNiO_3$-derived catalysts as dual function materials for CO_2 capture and in-situ conversion to methane, Fuel 320 (2022), 123842.
[70] P. Hongmanorom, J. Ashok, P. Chirawatkul, S. Kawi, Interfacial synergistic catalysis over Ni nanoparticles encapsulated in mesoporous ceria for CO_2 methanation, Appl. Catal. B: Environ. 297 (2021), 120454.
[71] H. Takano, Y. Kirihata, K. Izumiya, N. Kumagai, H. Habazaki, K. Hashimoto, Highly active Ni/Y-doped ZrO_2 catalysts for CO_2 methanation, Appl. Surf. Sci. 388 (2016) 653–663.
[72] L. Atzori, M.G. Cutrufello, D. Meloni, B. Onida, D. Gazzoli, A. Ardu, R. Monaci, M. F. Sini, E. Rombi, Characterization and catalytic activity of soft-templated NiO-CeO_2 mixed oxides for CO and CO_2 co-methanation, Front. Chem. Sci. Eng. 15 (2021) 251–268.
[73] M. García-Melchor, N. López, Homolytic products from heterolytic paths in H_2 dissociation on metal oxides: the example of CeO_2, J. Phys. Chem. C. 118 (2014) 10921–10926.
[74] K. Hadjiivanov, Identification and Characterization of Surface Hydroxyl Groups by Infrared Spectroscopy, in: Adv. Catal, 57, Academic Press, 2014, pp. 99–318.
[75] A. Solis-Garcia, T.A. Zepeda, J.C. Fierro-Gonzalez, Spectroscopic evidence of the simultaneous participation of rhodium carbonyls and surface formate species during the CO_2 methanation catalyzed by ZrO_2-supported Rh, Appl. Catal. B: Environ. 304 (2022), 120955.
[76] S.M. Lee, Y.H. Lee, D.H. Moon, J.Y. Ahn, D.D. Nguyen, S.W. Chang, S.S. Kim, Reaction mechanism and catalytic impact of Ni/CeO_{2-x} catalyst for low-temperature CO_2 methanation, Ind. Eng. Chem. Res. 58 (2019) 8656–8662.
[77] A. Cárdenas-Arenas, A. Quindimil, A. Davó-Quiñonero, E. Bailón-García, D. Lozano-Castelló, U. De-La-Torre, B. Pereda-Ayo, J.A. González-Marcos, J. R. González-Velasco, A. Bueno-López, Isotopic and in situ DRIFTS study of the CO_2 methanation mechanism using Ni/CeO_2 and Ni/Al_2O_3 catalysts, Appl. Catal. B: Environ. 265 (2020), 118538.
[78] M. Daturi, C. Binet, J.C. Lavalley, G. Blanchard, Surface FTIR investigations on $CexZr_{1-x}O_2$ system, Surf. Interface Anal. 30 (2000) 273–277.
[79] M.L. Ang, U. Oemar, E.T. Saw, L. Mo, Y. Kathiraser, B.H. Chia, S. Kawi, Highly active Ni/xNa/CeO_2 catalyst for the water–gas shift reaction: effect of sodium on methane suppression, ACS Catal. 4 (2014) 3237–3248.
[80] A. Trovarelli, Catalysis by ceria and related materials, J. Am. Chem. Soc. 124 (2002) 12923–12924.
[81] M. Li, T.H.M. Pham, E. Oveisi, Y. Ko, W. Luo, A. Züttel, Revealing the surface chemistry for CO_2 hydrogenation on Cu/CeO_{2-x} using near-ambient-pressure X-ray photoelectron spectroscopy, ACS Appl. Energy Mater. 4 (2021) 12326–12335.
[82] P.A.U. Aldana, F. Ocampo, K. Kobl, B. Louis, F. Thibault-Starzyk, M. Daturi, P. Bazin, S. Thomas, A.C. Roger, Catalytic CO_2 valorization into CH4 on Ni-based ceria-zirconia. Reaction mechanism by operando IR spectroscopy, Catal. Today 215 (2013) 201–207.
[83] M. Daturi, E. Finocchio, C. Binet, J.C. Lavalley, F. Fally, V. Perrichon, Study of bulk and surface reduction by hydrogen of CexZr1-xO2 mixed oxides followed by FTIR spectroscopy and magnetic balance, J. Phys. Chem. B. 103 (1999) 4884–4891.
[84] H. Tsuneoka, K. Teramura, T. Shishido, T. Tanaka, Adsorbed species of CO_2 and H_2 on Ga_2O_3 for the photocatalytic reduction of CO_2, J. Phys. Chem. C. 114 (2010) 8892–8898.
[85] X. Wang, Y. Hong, H. Shi, J. Szanyi, Kinetic modeling and transient DRIFTS–MS studies of CO_2 methanation over Ru/Al_2O_3 catalysts, J. Catal. 343 (2016) 185–195.
[86] Q. Pan, J. Peng, S. Wang, S. Wang, In situ FTIR spectroscopic study of the CO_2 methanation mechanism on Ni/$Ce_{0.5}Zr_{0.5}O_2$, Catal. Sci. Technol. 4 (2014) 502–509.